Multi-scale spatial distribution of K, Th and U in an Archaean potassic granite: a case study from the Heerenveen batholith, Barberton Granite-Greenstone Terrain, South Africa

Jean-François Moyen, M. Cuney, David Baratoux, Paul Sardini, S. Carrouée

▶ **To cite this version:**

Jean-François Moyen, M. Cuney, David Baratoux, Paul Sardini, S. Carrouée. Multi-scale spatial distribution of K, Th and U in an Archaean potassic granite: a case study from the Heerenveen batholith, Barberton Granite-Greenstone Terrain, South Africa. South African Journal of Geology, 2021, 124 (1), pp.53-86. 10.25131/sajg.124.0005 . hal-04123480

HAL Id: hal-04123480
https://hal.science/hal-04123480v1

Submitted on 7 Feb 2025

HAL is a multi-disciplinary open access archive for the deposit and dissemination of scientific research documents, whether they are published or not. The documents may come from teaching and research institutions in France or abroad, or from public or private research centers.

L'archive ouverte pluridisciplinaire **HAL**, est destinée au dépôt et à la diffusion de documents scientifiques de niveau recherche, publiés ou non, émanant des établissements d'enseignement et de recherche français ou étrangers, des laboratoires publics ou privés.

Multi-scale spatial distribution of K, Th and U in an Archaean potassic granite: a case study from the Heerenveen batholith, Barberton Granite-Greenstone Terrain, South Africa

Moyen, Jean-François[1,2,*]
Cuney, Michel[3]
Baratoux, David[4]
Sardini, Paul[5]
Carrouée, Simon[1]

1. Université de Lyon, Laboratoire Magmas et Volcans, UJM-UCA-CNRS-IRD, 23 rue Dr. Paul Michelon, 42023 Saint Etienne, France.
2. *On sabbatical at* School of Earth, Environment and Atmosphere Sciences, Monash University, Clayton, VIC 3168, Australia.
3. Université de Lorraine, CNRS, CREGU, GéoRessources, F-54000 Nancy, France
4. Géosciences Environnement Toulouse, Université Paul Sabatier & IRD, 14, Avenue Edouard Belin, 31 400, Toulouse, France.
5. Université de Poitiers, IC2MP/HydrASA, UMR 7285 CNRS, 86000 Poitiers, France

[*] Corresponding author. jean.francois.moyen@univ-st-etienne.fr

Abstract

We describe the multi-scale distribution of K, Th and U in the ca. 3.1 Ga Heerenveen batholith of the Barberton Granite-Greenstone Terrain. Data were obtained with a combination of tools, from the scale of the whole batholith (using car-based gamma-ray spectrometry) to outcrops (hand-held gamma-ray spectrometry and outcrop mapping), to thin section (alpha autoradiography). We describe the distribution of elements: U is concentrated preferentially in minor phases in the border shear zones of the batholith, and within these shear zones in late pegmatites as well as in fractures. We discuss the processes of U concentration and fractionation: U is concentrated by a combination of processes from magmatic (some rock types are intrinsically U-richer than other) to hydrothermal (redistribution of U in small fissures associated with magmato-hydrothermal fluids), and is dispersed by supergene alteration. Finally, we comment on the statistic properties of K, Th and U distribution: whereas K shows a strongly spatially controlled repartition, largely mirroring mappable rock types, and with increasing variability at larger scales, U, in contrast, is dominated by small-scale variations ("nugget effect") and its variability is, if anything, averaged and smoothed by large scale integration. Spatial and statistic features thus offer better insight on petrogenetic and metallogenic processes in granitoids.

1. Introduction

Geochemistry has become the *de facto* standard tool to investigate igneous processes, and it is unthinkable today to carry out a petrological study that does not include whole rock analyses (if only as a baseline for more sophisticated approaches). Geochemical analyses are, for the most part, treated using projections (binary and ternary diagrams). The trends are interpreted in terms of processes such as partial melting, magma mixing, crustal contamination, fluid-rocks interactions or crystallization.

However, binary and ternary diagrams are not the only way to analyse geochemical datasets (Aitchison, 1986; Pawlowsky-Glahn and Egozcue, 2006). In particular, geochemical datasetshave statistical properties including univariate (i.e. frequency distributions), multivariate (relations between more than 2 or 3 variables), and spatial properties (spatial dependence of concentrations of chemical elements). A handful of theoretical studies have proposed that these properties may reflect the superposition of elementary geochemical processes operating during magmatic processes and fluid-rock interactions affecting crustal rocks (De Wijs, 1951, Allegre and Lewin, 1995, Agterberg, 2012). Some case studies (Allegre and Lewin, 1995; Fall et al., 2018) have described log-normal distributions in intrusive bodies. Rarer works (e.g., Tartèse et al., 2011; Fall et al., 2008, in press) have attempted to discuss the spatial patterns of chemical properties of granitic intrusions in terms of geological processes. Another aspect seldom considered is the question of scale. This question of scales of mineralogical and chemical heterogeneities has appeared recently critical to the integration of in-situ and remote sensing data in the exploration of rocky planets (Yokoyama et al. 2015; Greenberger et al. 2020). Geochemical studies on Earth generally assume that samples are representative of a geological unit, or assume that the investigated unit is homogeneous at a given scale. Remote sensing techniques (gamma-rays surveys, hyperspectral data), or hand-held portable instruments (Field portable Gamma-Ray spectrometers, X-ray Fluorescence Portable Spectrometers, or portable LIBS - for “Laser-Induced Breakdown Spectroscopy) provide constraints on the chemistry of material exposed at the surface at scales from microns to hundreds of kilometers. Nevertheless, insufficient knowledge of scale-dependence of observations hinders the integration of data sets obtained with different analytical techniques. In petrological studies, the representative scale of a geochemical dataset is rarely specified. Is it the scale of the hand-specimen, of the outcrop or of the pluton? It is also obvious that igneous rocks are heterogeneous, to various degrees, at all scales. For instance, granitoids are made of

millimeter- to centimeter-sized mineral grains. At this scale, a chemical analysis may be representative of the composition of the mineral (except for chemical elements showing zonation) but not of the rock itself. Many outcrops include veins of aplites or pegmatites, heterogeneities such as schlieren or other mineral accumulations, enclaves, etc., which may result in compositional differences between samples distant a few meters or tens of meters from each other. Implicitly, it follows that a typical rock sample is representative at a scale of 1 to 10 m. In this work, we wish to explicitly explore the two following aspects: the representative scale of geochemical analyses, and the statistical properties of elemental distribution in a granitic complex.

Amongst the geochemical elements that one may trace, uranium is of particular importance because of its use as a multipurpose geochemical tracer, and its economic interest. Ore deposits are, ultimately, an extreme geochemical enrichment of metallic elements within a rock unit, controlled by common geological processes occurring in restricted regions of the crust. Thus, the study of the statistical properties in the crust of chemical elements of economic interest (such as U) is intrinsically related to the exploration for mineral resources and to the distribution of ore deposits. Many of the geochemical techniques used in this paper are borrowed from exploration geology. Uranium is radioactive, and its disintegration chain includes alpha, beta and gamma emitters, allowing for a range of detection tools in a multi-scale study.

A relatively quick way to assemble geochemical datasets amenable to such studies is through the use of gamma-ray mapping (for K, Th and U only, in natural conditions on Earth). Airborne radiometric datasets are commonly used for mapping, in particular in areas with poor exposure, such as densely vegetated and/or weathered surfaces in tropical regions (Dickson and Scott, 1997; Bierwirth and Brodie, 2008; Metelka et al., 2011; Tartèse et al., 2011; Xhixha et al., 2016; Elkhateeb and Abdellatif, 2018). Radiometric mapping allows mapping of the distribution of ^{238}U, ^{232}Th and ^{40}K, based on the assumption of equilibrium of the gamma emitters in their respective decay chains. K, Th and U are incompatible elements and tend to be enriched in the most felsic magmas, but their behaviours differ in details and vary with circumstances. For instance, U may be fluid-mobile, and in low-temperature peraluminous felsic melts, Th (similarly to Zr and REE) becomes compatible, because of saturation in accessory phases such as monazite (e.g. Watson and Harrison, 1983; Montel, 1993; Kelsey et al., 2008; Boehnke et al., 2013; etc.). These elements can therefore be used to investigate the effects of a range of geochemical behaviours.

Furthermore, it is, of course, possible to analyse the concentrations of K, Th and U in hand specimens, or to map them at the scale of a thin section, e.g. by autoradiography, and thus to produce multi-scale maps of the distributions of U, Th and K in granitic bodies (Cuney and Kyser, 2015; Cuney, 2020). The cost of airborne gamma-ray mapping depends on the line spacing (effectively, the resolution); with a typical line spacing of 50 m it works out to be in the region of ~ZAR 1000 / km^2, which is prohibitive (in the academic sphere). Hand-held gamma-ray spectrometers are robust and reliable devices that can be used to build "low tech" radiometric datasets on more limited areas but with a higher resolution, thus allowing the exploration of scales intermediate between rock samples, and intrusive bodies, encompassing the typical sales of outcrops.

Here, we apply these techniques to the ca 3.1 Ga Heerenveen Batholith in the Barberton Granite-Greenstone Terrain (BGGT), South-Africa, the smallest body in the GMS (Granite-Monzogranite-Syenite) suite. The Heerenveen Batholith offers an interesting case study for several reasons. Firstly, for practical reasons: the batholith has benefited from extensive sampling, with ca. 150 whole-rock analyses available, most of them georeferenced (Anhaeusser and Robb, 1983; Clemens et al., 2010; Moyen et al., in press). In addition, its southern portion is occupied by a commercial forest, crosscut by a dense network of unsurfaced forestry tracks. It is, therefore, possible to quickly obtain radiometric map by driving a gamma-ray spectrometer along these roads. Good, well-exposed outcrops, up to 100 m across, also provide the opportunity for small-scale lithological and radiometric mapping. It is thus possible to map the distribution of U, Th and K at scales ranging from tens of kilometers, to meters, and thin section studies allow to expand this range down to the micrometer-scale.

A further question regarding the GMS suite is its role in Earth's metallogenic evolution, specifically as a source for early U deposits. The oldest economic uranium deposits on Earth are the quartz pebble conglomerates (QPC) within the Kaapvaal craton in South Africa (Duhamel, 2010). Conglomerates from the sedimentary Rhenosterspruit formation of the Dominion Group (3086 ± 3 Ma to 3074 ± 6 Ma; Marsh, 2006) and from the Central Rand Group of the Witwatersrand Supergroup (2970 to 2780 Ma; Robb and Meyer, 1995; Robb et al., 1997) contain uraninite. The origin of the gold and uranium mineralization in the QPC remains controversial (Phillips and Law, 1997; Cuney, 2010; Depiné et al., 2013). However, there is a consensus that a critical role was played by the low level of oxygen in the atmosphere before 2.2 Ga (Krupp et al., 1994; Minter, 2006; Partin et al., 2013), allowing the preservation of

tetravalent uranium, such that uraninite crystals eroded from uranium-rich granitic rocks could be transported as detrital grains and concentrated in placers. Furthermore, the geochemical characteristics (Th and REE contents and patterns) of the uraninite grains in the Dominion and Witwatersrand deposits indicate a high-temperature crystallisation of these minerals, and consequently suggest a magmatic origin (Cuney, 2010; Rantzsch et al., 2011; Depiné et al., 2013). To explain the presence of detrital uraninite in the QPC deposits requires the presence of magmatic rocks sufficiently enriched in U and in which specific fractionation processes have permitted a decoupling of the two strongly incompatible Th and U, yielding sufficiently low Th/U ratios to crystallize magmatic uraninite. The K-rich GMS suite of Barberton (as opposed to Na-rich TTGs) is a good candidate for a potential source of this uraninite.

The Heerenveen batholith is made of a collection of magmatic phases with both an homogeneous core of megacrystic granite, and border shear zones containing a collection of meter- to 100s of meter-sized bodies of diverse rock types (Anhaeusser and Robb, 1983; Belcher and Kisters, 2006a, b). This spatial variability offers an excellent opportunity to investigate its effects both within, and between rock types.

In this paper, we address the "where", "what" and "how", and specifically investigate three complementary questions: (i) *Where* is uranium (and K and Th, to a lesser degree) located in the Heerenveen batholith? (ii) *What* are the processes responsible for U concentration and fractionation? (iii) Do the *statistical properties* of element distribution reflect the differentiation processes? We address these questions with a particular emphasis on the scale of observation, and show the additional information that can be derived by taking into account statistical univariate and spatial properties.

2. Geological setting

2.1 The Barberton Granite—Greenstone terrain

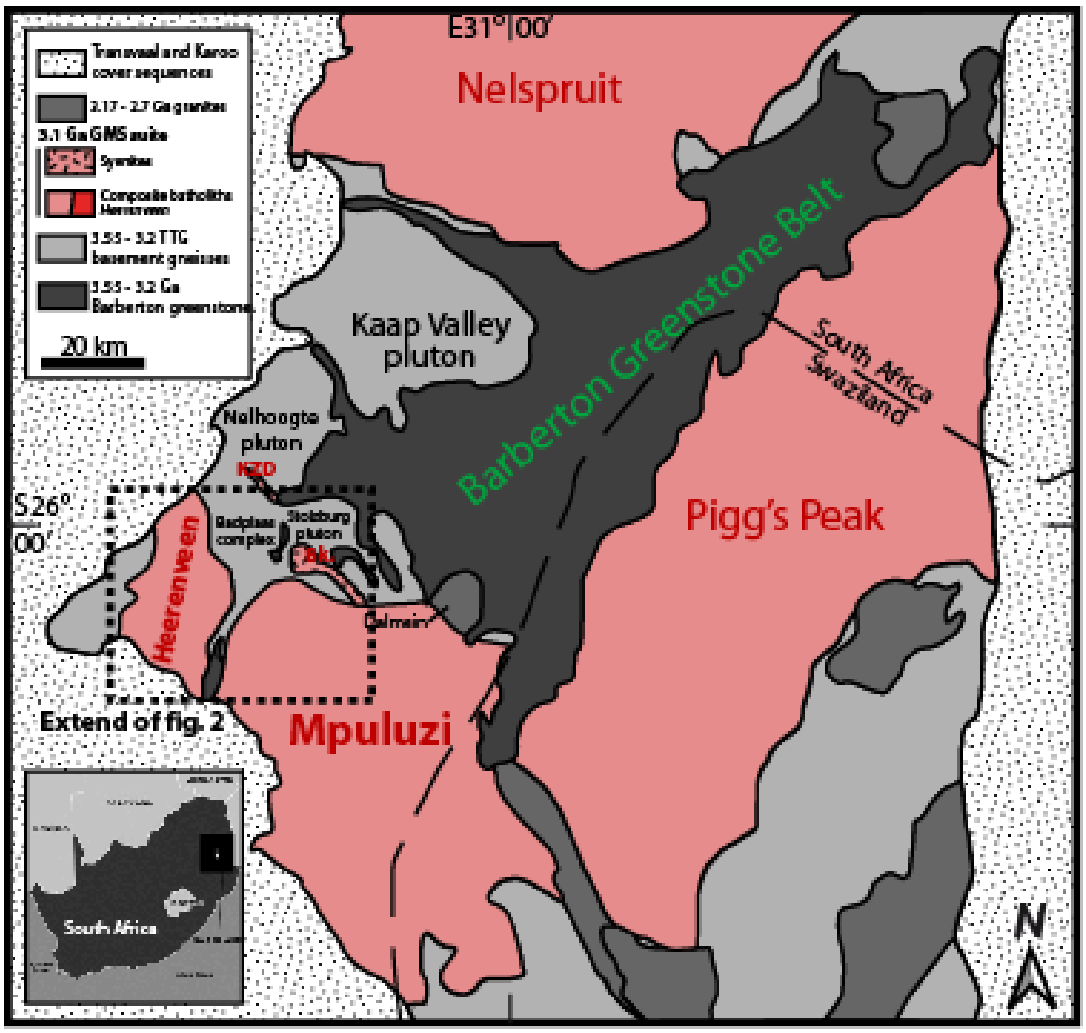

Figure 1. Simplified geological map of the Barberton Granite Greenstone Terrain, with emphasis of the GMS batholiths and syenites. Bk. : Boesmanskop syenite ; KZD : Kees Zyn Doorns syenite.

The mid-Archaean (3550 – 3150 Ma) Barberton Greenstone Belt (Figure 1) is surrounded by plutons belonging to the TTG suite (3500 – 3200 Ma; review in Moyen et al., 2018). The TTG plutons are intruded by the ca. 3110 Ma GMS (granite-monzogranite-syenite) suite, which consists of four dominantly granitic laccolithic intrusions: the Nelspruit Batholith to the North, the Pigg's Peak to the South-East, the Mpuluzi to the South, and the Heerenveen to the South-West (Anhaeusser and Robb, 1982; Jackson and Robertson, 1983; Robb et al., 1983). The Suite also contains small syenitic bodies (Boesmanskop, Veergevonden and Kees Zyn Doorns), coeval with the larger batholiths (Anhaeusser et al., 1983) (Figure 2).

This paper focuses on the Heerenveen Batholith and the adjacent portions of Mpuluzi and Boesmanskop intrusions, because (i) of its manageable size and (ii) good exposure and access conditions, and (iii) of the presence of a well-understood geological, geochronological and geochemical background, a detailed account of which is given in a companion paper (Moyen et al., in press).

2.2 The Heerenveen and Mpuluzi Bbatholiths geology and petrogenesis

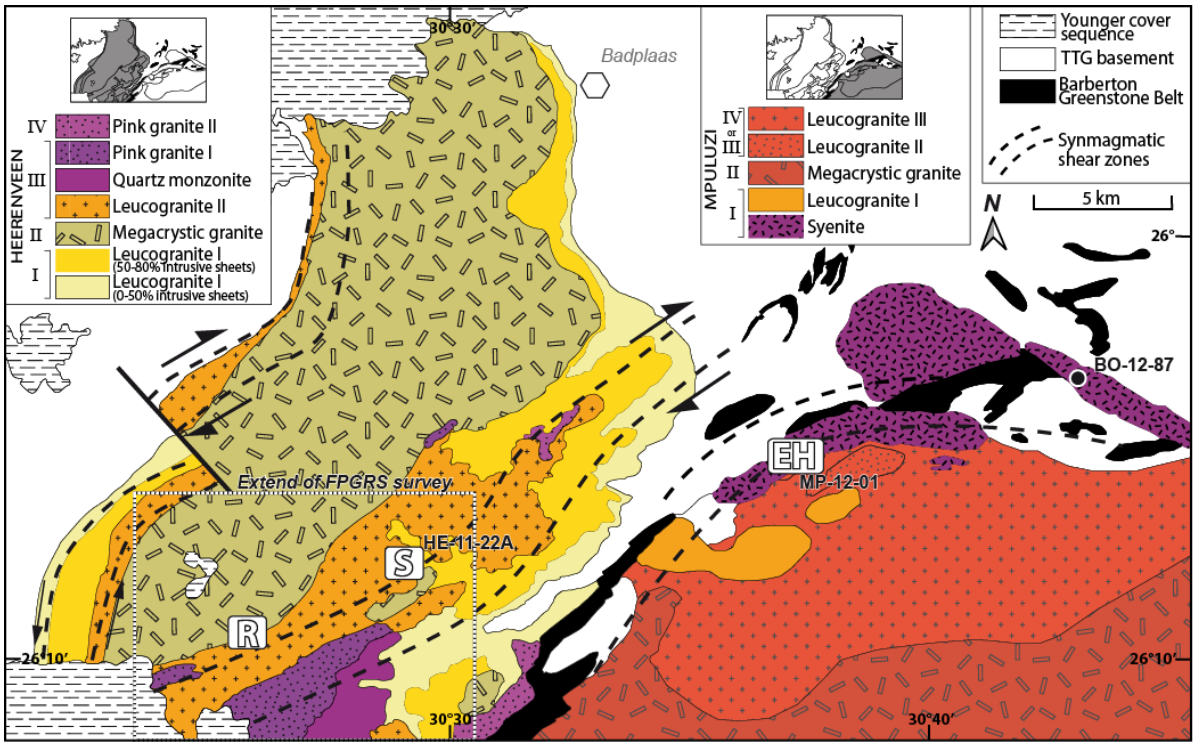

Figure 2. Geological map of the Heerenveen Batholith and adjoining portions of the Mpuluzi Batholith (Modified from Moyen et al., in press). Heerenveen after Belcher and Kisters (2006a ; b); Mpuluzi after Westraat et al. (2005). EH : Eagle High locality (Figure 10). R : « River » locality (Figure 8). S : « Steep » locality (Figure 9). The extent of the gamma-ray survey (corresponding to Figure 7) is also indicated, as well as the location of BeaQuant sample BO-12-87 of the Boesmanskop syenite (black circle, in the eastern part of the figure).

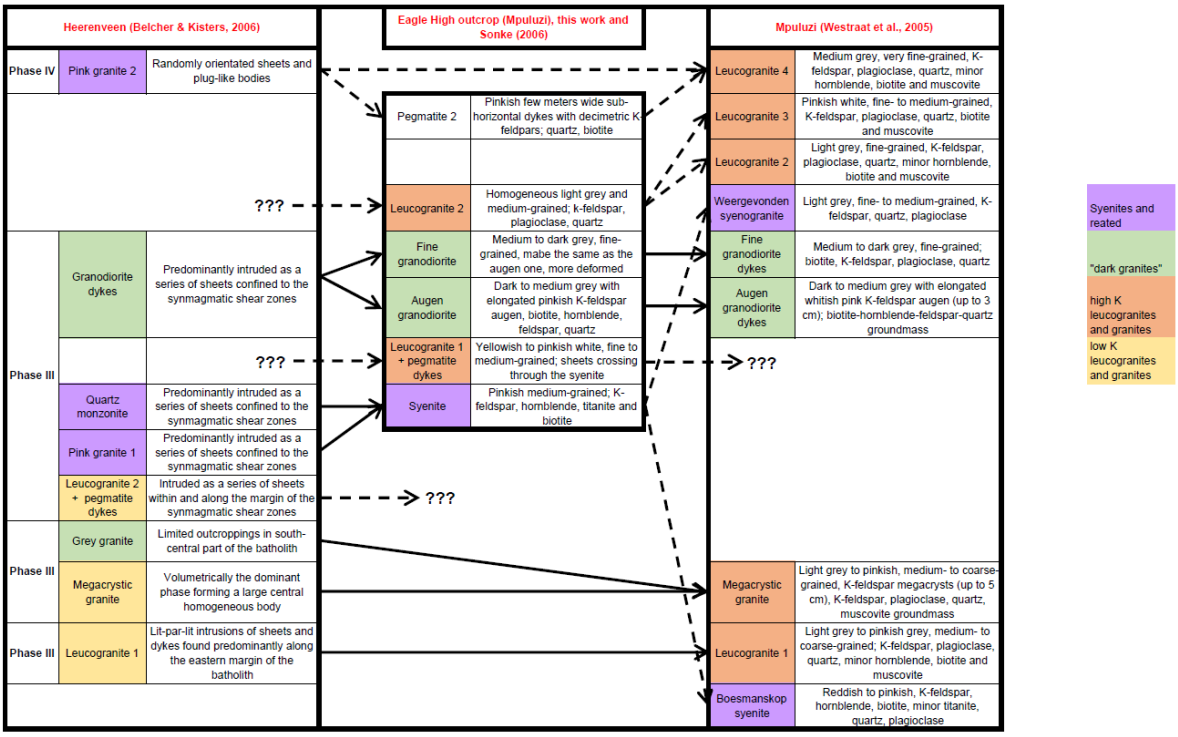

Table 1. Correlation between Heerenveen and Mpuluzi facies. Heerenveen after Belcher and Kisters (2006a, b). Mpuluzi margin (Eagle High outcrop, loc. EH on Figure 2) after Sonke (2006) and this work. Inner portions of Mpuluzi after Westraat et al. (2005). The different facies are colour-coded according to their chemical grouping.

Field relations, petrography and geochemistry of the Heerenveen Batholith (and adjacent units) are reported respectively by Belcher and Kisters (2006a, b), Clemens et al. (2010), and Moyen et al. (in press). The key points are summarized here.

The Heerenveen Batholith (and nearby units) is a composite body made of several petrographically and chemically distinct rock types, forming distinct map units. All of the units emplaced synchronously within error (ca. 3110 Ma), and share similar isotopic characteristics (ε_{Hf} ca -1 to -2; Moyen et al., in press).

Field relations nonetheless allow establishing a chronology of emplacement for the Heerenveen Batholith (Table 1). It is composed of 8 different facies belonging to 4 main phases of intrusion: (phase I) a first sheet-like leucogranite (*leucogranite 1*) emplaced into the gneissic basement and was followed by (phase II) the intrusion of a homogeneous, weakly deformed, large body of porphyritic granite (*megacrystic granite*), the main phase in the Heerenveen and Mpuluzi Batholiths (Fig. 3a). This was accompanied by minor occurrences of a *grey granite*, and

followed (phase III) by the emplacement of a series of smaller, strongly deformed bodies in the bounding shear zone. They comprise a second leucogranite (*leucogranite 2*), a *quartz-monzonite* (Fig. 3b), a pink granite (*pink granite 1*), and dykes of *granodiorite*. The final phase (phase IV) consists of the post-tectonic intrusion of a second undeformed pink granite (*pink granite 2*). The Mpuluzi and Heerenveen Batholiths are separated by the Mkhomazane valley and may belong to the same intrusive complex. Westraat et al. (2005) mapped the North-Western portion of the Mpuluzi Batholith (Figure 2). In general terms, the relative chronology of emplacement in North-Western Mpuluzi seems to match the phases mapped in Heerenveen. As in the Heerenveen Batholith, the latest phases of the Mpuluzi Batholith emplaced into a syn-magmatic shear zone (the Weltverdiend Shear Zone, WSZ: Westraat et al., 2005).

Petrographically and chemically, three main groups can be identified. The most common rock type (> 90 %) is comprised of all the *leucogranites* and *megacrystic granites* of both batholiths. They range from granodiorite to leucogranite, mostly have SiO_2 > 71 % and are weakly peraluminous. Moyen et al. (in press) subdivided them into three sub-groups, low, medium and high-K, with the Heerenveen leucogranites & granites being chiefly low-K, whereas the Mpuluzi granitoids are mostly high K. Collectively, these features can be ascribed to partial melting of a composite grey gneisses source, yielding a range of magma batches, some of which underwent further differentiation (Moyen et al., in press).

The *syenites*, *monzonites* and *pink granites 1 and 2* define a second group, making up perhaps 5-10 % of the total outcrop. They commonly include hornblende and/or titanite, and define a fairly long magmatic series, from ca. 60 to 70 % SiO_2, invariably K-rich (5 – 6 % K_2O even for the lower SiO_2 terms). They are mostly metaluminous and ferroan *sensu* Debon and Lefort (1983). The third group of "dark granitoids" (*grey granite* and *granodiorite*) includes small volumes (< 1 %?) of rocks that form small dykes, enclaves, etc., typically too small to be mapped at the regional scale, although they form a significant portion of some outcrops, e.g. the Eagle High outcrop described below. They have 60-65 % SiO_2, and define several series ranging from a low-K, weakly peraluminous series to a high-K, metaluminous series. Collectively, both the syenites and the dark granites can be interpreted as belonging to several differentiation series rooted in magmas formed by partial melting of a mantle enriched by the incorporation of crustal material – isotopically analogous to the regional crust (Moyen et al., in press). Chemical variations between all these magmas can be ascribed to different contaminants, varying degrees of contamination and/or degrees of melting of the mantle.

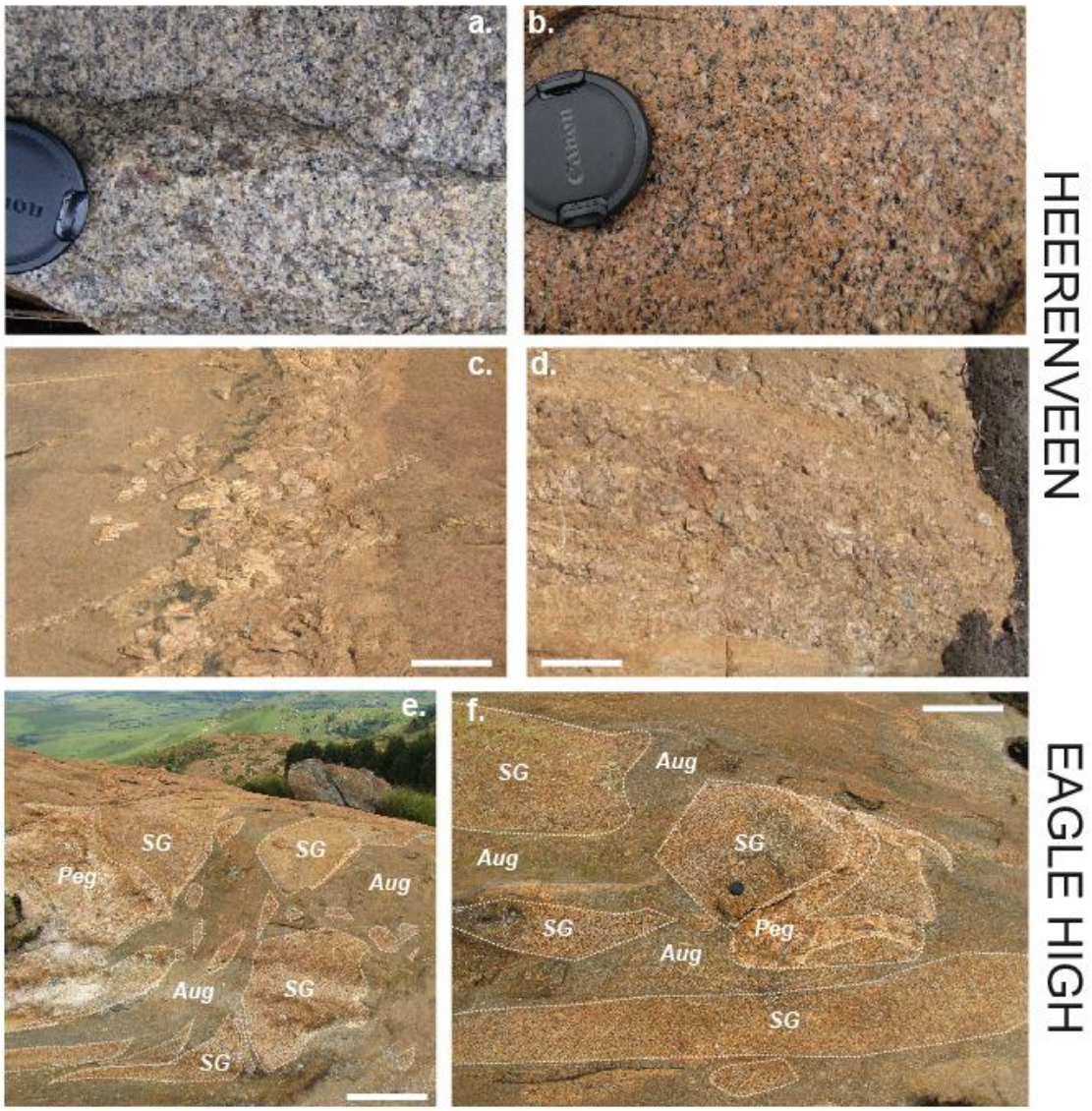

Figure 3. Field photographs of representative lithologies. (a). Homogeneous granite of the main Heerenveen megacrystic granite. (b). Pink monzonite of the Heerenveen batholith. (c) and (d) Dilacerated pegmatites in *leucogranite 2* (« river » locality, Figure 8). (e-f). Field relations at the Eagle High locality (Figure 10) : Clast of syenogranite to syenite (SG), associated with an early, folded and truncated pegmatite (Peg), forms enclaves in an augen granodiorite (Aug), one of several types of "dark granitoids". Scale bar is ca. 20 cm in c, d and f and ca. 1 m in e. Lens cap (6 cm) for scale in a and b.

3. Tools and methods

3.1 Mapping and sampling

In this work, we rely on excellent existing regional and local mapping (Figure 2) to guide sampling. To investigate properties at the scale of meters to tens of meters, outcrop-scale mapping was performed on two key localities in the Heerenveen batholith that reconnaissance

studies identified as U-rich. In each case, we mapped a ca. 10 × 10 meter grid at a 1:40 scale. The "river" locality (near 26.1722°S, 30.4434°E; Jagtlust 30 IT; Fig. 3c-d) features several phases of leucogranites, injected with pegmatites. Both rock types are sheared together and physically mixed at the scale of the outcrop. The "steep" locality (26.1329°S, 30.4989°E; Kleintheespruit 28 IT) also contains sheared leucogranites, but here they are cut by prominent, post-tectonic pegmatites. For comparison, we mapped in detail a ca. 1150 m^2 section of the Eagle High outcrop (26.098°S, 30.629°E; Welgevonden 175 IT) in the Mpuluzi batholith, at a scale of 1:100. This spectacular outcrop, situated in the WSZ, contains a large variety of facies with clear interrelationships (Fig. 3e-f). A syenogranite is injected by a first set of leucogranite intrusions (*leucogranite 1*) associated with pegmatites (*pegmatite 1*), then intruded by an *augen granodiorite* and to a lesser extent by a *fine-grained granodiorite* (both varieties of the dark granitoids). To the East of the Eagle High outcrop, a large intrusion of a second leucogranite generation crops out (*leucogranite 2*), with deformed contacts with the previous facies. Some large dykes of a late pegmatite (*pegmatite 2*) cut all the previous facies. The Eagle High outcrop allows us to extend our survey to a wider range of phases.

Geochemical analyses for the Heerenveen Batholith exist for nearly 90 samples (Anhaeusser and Robb, 1983; Yearron, 2003; Belcher and Kisters, 2006a, b). Unfortunately, only the 34 samples from Belcher and Kisters are identified in terms of which phase they belong to; the other studies only describe them as "Heerenveen", although it is sometimes possible to retrieve this information from field descriptions and locations. The 43 samples analysed by XRF by Anhaeusser and Robb (1983) do not include U and Th contents. Sixty-six new samples were collected and analyzed in the course of this study. In the Mpuluzi Batholith, our 23 samples enlarge an existing database of 159 samples, also from a mixture of origins with correspondingly incomplete set of analysed elements. Thin sections were made from our samples, and the remaining material was crushed and milled in a chalcedony ring mill for whole rock chemical analyses that were performed at the SARM (CRPG-Nancy, France) using XRF for major elements, and ICP-MS for trace elements, using routine procedures. All analyses of the Heerenveen and Mpuluzi Batholiths used in this study are provided as Electronic Appendix 1.

3.2 Gamma-ray spectrometry

In this study, we used a hand-held gamma-ray spectrometer, to obtain continuous readings of U, Th and K concentrations and derive radiometric maps at the batholith and outcrop scale. To the best of our knowledge, while spectrometers are commonly used during mineral exploration, they are less commonly used for academic research (Fall et al., 2018, in press) and therefore this approach requires some methodological validation, depending on the specific type of hand-held gamma-ray spectrometer that is used.

A PGIS-21 spectrometer (courtesy of ORANO Group - France) with a 347 cm^3 (21 in^3) NaI crystal has been used here. The spectrometer is calibrated and maintained by ORANO following manufacturer's specifications, which are beyond the control of the end-user. The apparatus has a capacity of 65535 counts per channel, an energy detection range from 36 KeV to 3 MeV. The gamma-ray window used for retrieving K, Th and U concentrations are at 1.46 MeV for the ^{40}K, 1.764 MeV for the ^{214}Bi, a decay product of the ^{238}U, and 2.614 MeV for the ^{208}Tl, a decay product of the ^{232}Th. It is coupled with a GPS, allowing direct recording of measurements locations with a typical spatial accuracy of ± 2-3 m.

Gamma-rays are absorbed by the surrounding rock according to their energy: at 1.332 keV, 90% of the gamma-ray signal comes from about the first 17 cm (99% from the first 34 cm) (Mavi, 2012; Dentith and Mudge, 2014), the exact number being dependent on rock density (gamma-rays will reach deeper sections in porous or low-density rocks). The energies of the gamma-rays used to analyse K and U are close to each other; thus the analysed depth for these two elements should be similar. The gamma-rays used to measure Th concentrations are more energetic; thus Th is analysed to a slightly greater depth than U and K.

Using this spectrometer, the solid angle associated with the gamma-ray detector is 4π. Therefore, the size of the area from which a certain fraction of the gamma-rays is detected varies according to the altitude of the detector with respect to the ground. (Dentith and Mudge, 2014) and the contributions decrease continuously with distance to the measurement location. Assuming a point-like crystal and an infinite, flat surface, 90% of the signal comes from an area of ca. 50 cm radius when the crystal is 5 cm above ground level; at 20 cm, 80% of the signal comes from an area of 1-meter radius and 90% from an area of 2-meter radius. If the detector is at 50 cm above the ground, 80% of the gamma-rays come from an area of 2.5 m radius and 90% from a 5 m radius. These numbers explain the difficulty of analysing thin (centimetric) pegmatite dykes, because the counting is dominated by the surrounding rocks.

3.2.1 Modes of acquisition

We used the gamma spectrometer in three different modes. As the scale of measurement differs in each mode, the datasets obtained in different modes cannot be directly compared, but provide complementary information. The full datasets are given in full in Electronic Appendix EA3.

In **dynamic foot mode**, the spectrometer was held at 20 cm above the rock and carried on foot. This mode was used to explore the three outcrops for which we have detailed lithological maps (one in Mpuluzi and two in Heerenveen). In addition, data gathered during the reconnaissance of the Eagle High outcrop in dynamic foot mode also proved to be sufficiently dense to be exploited, giving insights into the distribution of the radioactive elements over an area of about 1 km^2. The spectrometer records one reading every second, roughly corresponding to every 50 cm at a normal walking pace. This is well below the GPS accuracy; therefore, the locations of the measurements were corrected using the mapping information to ensure that the data points were located in their correct positions.

In **dynamic car mode,** the spectrometer was laid down on the floor of the car and readings were recorded every second along the dense network of forestry tracks in the Southern Heerenveen batholith. The tracks are simply graded and scraped through the forest, with very little additional filling, such that most of the sand and gravel is effectively derived from local regolith. Unfortunately, the same approach was not feasible in the Mpuluzi batholith, due to topographic constraints: the edge of the batholith underlies a ca. 300 m high escarpment, whereas the core is largely used for local farming and the roads are either tar, or filled with sand and gravel from nearby quarries, and therefore unsuitable for this approach.

The floor of the car did absorb some of the gamma-rays. Detailed measurements of the effects of the floor of the car were not collected during the field campaign, so it is not possible to correct the measurements from this effect. Each element concentration will be affected by a different factor, as the correction is expected to be energy-dependent. These non-calibrated data are still useful to examine distances of auto-correlation (spatial statistics) and univariate statistics, keeping in mind that concentration values are affected by a constant factor that differs for each element. Therefore, bivariate statistics on these data should be avoided. One reading was taken every second, corresponding to a typical distance of about 10 m when driving at ca. 30 km/h. This is three times the GPS resolution; furthermore, typical traverses were two to five kilometre long, such that the small location error is relatively negligible.

In **static mode** the spectrometer was directly laid down on the rock surface. Readings of 30 s were taken for each spot. As detailed before, in this mode, approximately 90% of the radiation received by the detector comes from a 50 cm radius around it. Thus, we assume that, in static mode, the spectrometer measures concentrations approximately within a 1-meter diameter footprint, having however in mind that, in this 1-meter diameter, the measurement of gamma radiation is non-uniform. Static mode was mostly used to get better quality data on the two outcrops of the Heerenveen batholith that are mapped in detail. For one of them, the "Steep" outcrop, we took and averaged three readings at each node of the grid, further reducing the standard deviation, as we discuss below. Due to time constraints, it was not possible to perform the same work on the Mpuluzi outcrop, for which we only have "dynamic" readings.

3.2.2 Precision and accuracy

Precision: we assess here the quality of the spectrometer data in the static mode. Firstly, we evaluated the effect of the counting time. Fifteen measurements (five over 30 seconds, five over 60s and five over 120 s) were acquired on two different spots (of a fine-grained and coarse-grained granite respectively) located on a flat surface, to minimize geometric effects (Electronic Appendix 2). Differences between the mean of the five estimates of the concentrations obtained over 30 seconds and the five obtained over 120 seconds were ≤ 10%. The standard deviation of the measurements decreased and was roughly halved between 30 and 120 s, as predicted by statistics ($\sqrt{}$ (120 / 30) = 2). However, except in the case of very low concentrations, the standard deviation for 30s measurements is always < 10 %, and commonly close to 5 %. Thus, we mainly used 30 s analyses, bearing in mind that these come with an additional uncertainty of 10%. The precision might be affected by the temperature of the detector, but this effect was not examined here because our measurements did not involve large temperature fluctuations.

Accuracy: The accuracy of spectrometer measurements is estimated based on comparisons with whole rock analyses. This has been done by repeatedly analysing the same boulder with the spectrometer, ideally using the same location, following the protocol detailed below, and then analysing a fragment of "the same rock". Boulders were selected, rather than flat surfaces, owing to the obvious requirement to being able to physically break off a sample of the rock, but on the other hand, they have the disadvantage of a non-planar geometry. Thus, this

validation approach has two major limitations: the geometry of measurement may significantly affect the gamma-ray measurement, and the scales of the analyses differ by about three orders of magnitude in mass (~1 tonne for gamma-ray but only a few hundreds of grams for chemical analyses of the samples). Since the instrument is calibrated for measurements over a semi-infinite half-plane, the measurement on the convex surface of a boulder underestimates the K, Th and U concentration since fewer gamma-rays are counted, relatively to the same rock for a semi-infinite plane. The effect of scale should be considered, i.e. the volume of the rock samples, versus volume analysed by the spectrometer. This effect depends on the frequency distribution of K, Th and U within the integration volume of the spectrometer: for instance, if the distribution is normal, the probability of obtaining a lower or higher concentration in the rock sample than in the boulder is the same. If the distribution is log-normal, the probability of collecting a sample with a lower concentration than in the boulder-average is higher. Two contrasting rock types were selected: one from the Heerenveen's *megacrystic granite*, poorly enriched in incompatible elements (rock type "poor", 30.4177°E, l26.1213°S), and one from the Heerenveen's *quartz-monzonite* showing higher U, Th and K concentrations (rock type "rich", 30.4547°E, 6.1947°S).

We finally investigated the effects of using either "static" (30 s integration time) or "dynamic" (1 measurement every second) mode. Ninety-nine static analyses (30 seconds each) and 2105 dynamic analyses (1 second each) were taken on a 1×2 meter block of the Heerenveen *quartz-monzonite*, on a single occasion. Hundred and sixty static and 3920 dynamic analyses were taken on a 2×2 meter block of *megacrystic granite*, over 8 different days (20 static analyses per day) to check for any time-related deviation in the measured concentrations. Three samples on the *quartz-monzonite* block and two on the *megacrystic granite* block, surrounding the spots analyzed with the spectrometer were taken for whole-rocks analyses. These measurements are given in Table 2 and represented in Figure 4.

		"Poor" sample					
		K (%)	U (ppm)	Th (ppm)	Th/U	Th/K	K/U
Whole rock chemical analysis		**1.87**	**0.58**	**2.42**	**4.16**	**1.29**	**3.22**
Static	Average	2.63	1.73	5.17	3.00	1.97	1.52
	Standard deviation	*0.14*	*0.38*	*1.00*			
Dynamic	Average	2.64	1.73	5.32	3.07	2.02	1.52
	Standard deviation	*0.36*	*0.95*	*2.47*			
	Mode	2.46	1.24	4.52			

		"Rich" sample					
		K (%)	U (ppm)	Th (ppm)	Th/U	Th/K	K/U
Whole rock chemical analysis		**3.67**	**3.03**	**11.40**	**3.76**	**3.11**	**1.21**
Static	Average	4.85	4.88	15.65	3.21	3.23	0.99
	Standard deviation	*0.20*	*0.67*	*1.72*			
Dynamic	Average	4.85	4.84	15.67	3.24	3.23	1.00
	Standard deviation	*0.51*	*1.96*	*4.38*			
	50th percentile	4.99	6.35	14.59			

Table 2. Comparison between the results of chemical and gamma-ray analyses.

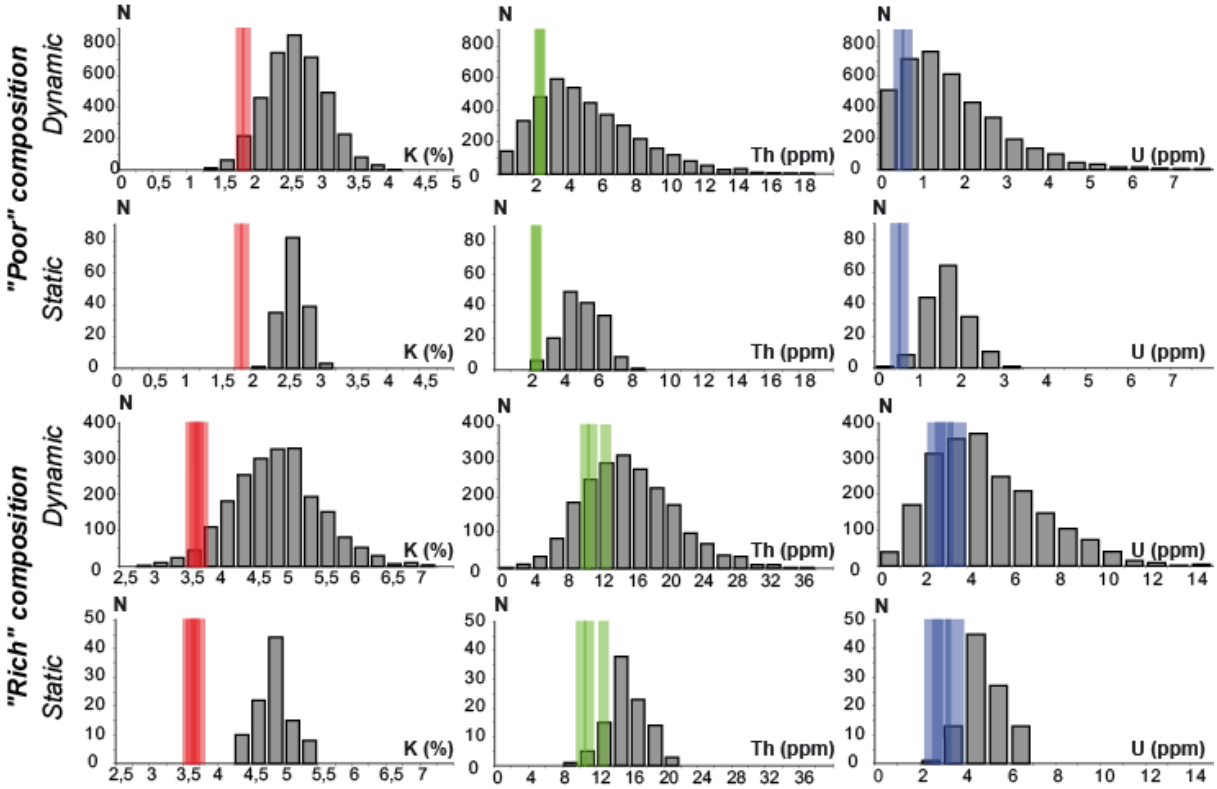

Figure 4. Comparison between the U, Th and K concentrations obtained by gamma-ray spectrometry (grey histograms) and those obtained by whole rock analysis (red, green and blue bars). Several rock fragments were analysed for each boulder, they are depicted by the overlapping, semi-transparent bars.

The contents obtained from whole-rock (chemical) analyses are systematically lower than those obtained with the spectrometer. Unfortunately, we do not have a sufficiently exhaustive control dataset to explore and understand this effect, nor do we have access to the manufacturer's calibration routines. However, the fact that the ratios are roughly consistent between the whole-rock analyses and the radiometric data suggests that a common explanation should explain the higher values reported by the portable spectrometer. This difference cannot be due to the

geometry (as this would produce an opposite effect). However it may be explained partially by the scale factor. If the volume measured by the spectrometer includes rare zones of elevated K, Th and U concentrations that were not sampled (nugget effect), the distribution would be log-normal (as commonly observed for incompatible elements at larger scales), and the larger-scale average should not match the average from a smaller sample. While log-normal distributions at this scale are plausible for U and Th, which are hosted in accessory minerals and possibly fractures (i.e. in small volume of the rock), this interpretation is questionable for K, which is hosted in major rock forming minerals (feldspars). On the other hand, the ratios between elements match the geochemical analyses more closely for the rich sample than for the poor one (Tab. 2).

As expected, the arithmetic means of the static and of the dynamic modes are similar, and only the standard deviation is higher in the dynamic mode. However, the reduction in standard deviation between dynamic and static mode is less than expected: averaging 30 measurements should reduce the standard deviation by a factor $\sqrt{30} \approx 5.5$. The observed improvement is closer to a factor 2 to 3.

The concentrations obtained accross several days show no systematic variation with time. K concentrations are stable (± 1 % between days) with higher variations in U and Th concentrations (± 10 % and ± 5 % respectively).

These experiments do not fully validate the accuracy of the portable field spectrometer against standard geochemical sampling, but they illustrate the order of magnitude of the differences that may be observed when comparing such data sets with geochemical databases, and the potential sources of differences that would require dedicated studies to be resolved. For this study, this suggests that going beyond semi-quantitative analyses is risky, especially when comparing different datasets.

3.3 Autoradiography

At the thin-section scale, uranium mapping was carried out using a novel autoradiographic technique (Beaquant™) based on the detection of alpha particles. The Beaquant™ instrument was initially developed in the bio-medical field and was adapted to low-energy beta particles emitted by tritium (Donnard et al., 2009a,b). It is based on the use of parallel ionization multipliers working in a proportional mode in a gaseous chamber (PIM - MPGD). Mapping

alpha particles emitted by geo-materials from a thin section involves the detection and localization of individual alpha particles that emerge from the thin section (Sardini et al., 2016). The counting of alpha particles is spatialised in a raster image file, each pixel intensity being equal to the number of alpha particles emerging at that pixel. The efficiency of counting is near 80% (Sardini et al., 2016). Autoradiography of alpha particles was recently applied for characterising mine tailings and materials derived from the dismantling of nuclear facilities (Angileri et al., 2018, 2020; Billon et al., 2019, 2020).

Five sections were investigated using the Beaquant™ (Table 3). Samples were initially selected using a radiometer (RadEye B20). Samples from Mpuluzi (MP) and Boesmanskop (BO) present an activity significantly higher than the background (about 3-4 times). In contrast, the samples from Heerenveen (HE) presented an activity very close to the background. Only one HE sample was selected. Two thin sections come from the "steep" outcrop (HE-11-22) and one from the "Eagle High" outcrop (MP-12-01_1 and MP-12-021). Another two (BO-12-07_1 and BO-12-07_2) correspond to small chips sampled from a U-rich spot identified during fieldwork in the Boesmanskop syenite, and not further studied. The output maps are given in Electronic Appendix EA4.

Converting alpha counts to U concentrations relies on two assumptions: (1) the ^{238}U series is at secular equilibrium, and (2) the alpha emissions come only from the ^{238}U series (neglecting ^{232}Th and ^{235}U series). ^{235}U is a minor isotope (< 1 %), but ignoring ^{232}Th is a strong assumption because Th/U ratios of the investigated rocks range from 0.3 to 10, meaning that a significant portion of the alpha comes from Th. It is unfortunately unavoidable because the instrument does not yet allow separating the alpha emissions according to the series from which they come. As the activity of ^{232}Th is about only a quarter the activity of ^{238}U, the implications of this assumption are mitigated.

Following this, for each pixel (i,j) of the alpha emission map, the alpha counting rate Nα(i,j) (cps/mm^2) was taken proportional to the U content, U(wt%)(i,j) (ppm), using:

$$U(wt\%)(i,j) = N_{\propto}(i,j) \times \frac{U(wt\%)(UO_2)}{N_{\propto}(UO_2)} \qquad \text{[eq. 1]}$$

where U(wt%)(UO_2) and Nα(UO_2) (cps/mm^2) are the U content (ppm) and the alpha counting rate (cps/mm^2) of uraninite, respectively. These two parameters were taken from Sardini et al. (2016): U(wt%)(UO_2) = 7x10^5 ppm and Nα(UO_2) = 2.3 cps/mm^2. Hence, the correction factor applied with these settings and total counting time (248743 s) is such that a count of 100 alpha

particles in a 100 x 100 µm^2 pixel over 248743 seconds corresponds to ca. 12235 ppm U in the pixel.

sample Name	Area mm^2	counting -	Activity cps/mm^2	U(wt%) ppm	U (WR) ppm
BO12-07_2	686,8	254054	1,48E-03	452	588
BO12-07_1	836,5	70215	3,37E-04	102,7	588
MP12-01_1	797,2	92160	4,65E-04	141,4	400
MP12-01_2	482,8	46595	3,88E-04	118,1	400
HE11-22-A	833,6	1805	8,70E-06	2,65	5.904
BCKG1	803	168	8,40E-07	0,26	
BCKG2	5205	2083	1,60E-06	0,49	

Table 3. Counting of alpha particles, surface activity and U content measured using BeaQuant™ on five thin sections. Total counting time is 248743 seconds. The areas of ROI (regions of interest) are indicated in column two. Two measurements of the background (BCKG 1 and BCKG 2) are provided at the bottom of the table. The analysed composition of an equivalent whole-rock samples is given in the last column (labelled WR).

One rock fragment was analysed for each sample (even though several thin sections have been cut from some samples), for practical reasons (amount of material available for analysis). Comparing the concentrations over the whole thin section with analysed samples (Table 3) reveals reasonable consistency. In most cases, the rock fragments analysed have U contents similar to the thin sections studied for autoradiography, with the exception of BO-12-07_2 which contains ca. 100 ppm U, i.e. significantly less than the 588 ppm found in the corresponding rock chip. This in itself suggests that, in this sample at least, heterogeneities exist on a scale a few centimetres (the concentration of U varies by a factor of 5 in initially adjacent cm-sized rock fragments).

3.4 Electronic microscopy

Key thin sections were imaged using a scanning electron microscope. Reconnaissance mapping of fifteen samples with low Th/U was performed at Laboratoire Magmas et Volcans, Clermont-Ferrand, France using a Jeol JSM 5910 LV microscope operated at 15 kV, with a Si(Li) EDS detector coupled with the PGT's Spirit system for semi-quantitative analyses and chemical mapping. Imaging of the whole thin sections previously investigated by BeaQuant was performed at IC2MP, Poitiers, France using a Jeol JSM-IT-500 SEM. We used the backscattered electron mode to image the mineral phases. These images at thin-section scale

were obtained by digital stitching of smaller images (magnification × 55, 1280 × 960 pixels, integration time 0.5 s).

525

3.5 Statistics and spatial analysis

The gamma–ray data and, to some degree, the whole rock batholith-scale data were analysed using three groups of statistic: univariate statistics, characterising the distribution of one
530 variable (one element) without any spatial consideration; bivariate statistics, investigating the co-variations of two elements –i.e. conventional geochemical plots—, and spatial analysis, aiming at describing the spatial distribution of the concentration of one element. Data and script are available as Electronic Appendix EA5.

535 Univariate statistics are reported (Electronic Appendix EA6) for each analysed element (K, Th and U) in the form of probability density curves, estimated by KDE (Kernel Density Estimate; Rosenblatt, 1956; Parzen, 1962), with a bandwidth selected according to Silverman's 'rule of thumb' (Silverman, 1986), as implemented in the statistical package R (Venables and Ripley, 2002). For each density curve, additional statistics are also given: the mean, the median, the
540 mode (concentration corresponding to the highest frequency), the standard deviation, the relative standard deviation, the skewness and kurtosis. The skewness is an estimate of the asymmetry of the distribution (skewness = 0 for symmetrical distributions) whereas kurtosis indicates the importance of the "tail" (occurrence of frequent/extreme outliers) of the distribution (kurtosis = 3 for a Gaussian distribution).

545

Bivariate statistics are used primarily in the form of conventional, bivariate geochemical plots that form the basis of the interpretation presented in section 5.

Spatial statistics (Electronic Appendix EA7) are based on the estimation of empirical
550 (semi)variograms, corresponding to the variance between each possible pair of measurements at a given distance from each other (Cressie, 1992). The variogram indicates the average degree of dissimilarity between samples at a given distance (or lag). In most cases, the variance increases until a plateau is reached (the "sill" of the variogram), indicating that all the possible diversity in the dataset is sampled at that distance. The number of pairs of points available for
555 each distance decreases when the lag reaches half of the size of the studied domain, at which

point the variogram becomes less robust. Variograms were calculated using the R package *gstats* (Pebesma, 2004) for lag ranges that depend on the dataset used, its spatial coverage and its spatial density of measurements.

Variograms are also used as input for interpolation of our data using ordinary block kriging. The interpolated grid, by construction, has the same spatial properties as the underlying variogram (specifically, of an analytical representation of the empirical variogram, inferred from the data and fitted to a given mathematical equation, the "model variogram"). The model variograms used for kriging our data are indicated in the respective figures (Electronic Appendix EA7); the parameters are determined to fit the experimental variograms. The models include an anisotropy component, mimicking the actual regional trends. Model variograms obtained from our data are plotted, and their fitting parameters are reported. The interpolated grids (together with an R script allowing generation of the plots) are supplied in Electronic Appendix EA5.

4. Datasets and scales of observation

Dataset	Locality / geological unit	< Sample size>	< Spacing >	Area	Method	Elements	Comment
WR Heerenveen	**Whole Heerenveen**	**10 cm**	**1891 m**	**432 km2**	**WR chemistry**	**majors, incomplete traces**	**Irregular grid**
WR Boesmanskop Megacrystic	**Megacrystic granite**	**10 cm**	**1675 m**	**47.1 km2**	**WR chemistry**	**majors, incomplete traces**	**Irregular grid**
WR Mpuluzi	**Whole Mpuluzi**	**10 cm**	**3929 m**	**1333.9 km2**	**WR chemistry**	**majors, incomplete traces**	**Irregular grid**
Gamma- ray Heerenveen	**Southern Heerenveen**	**10 m**	**69.8 m**	**108.6 km2**	**Gamma-ray, dynamic mode (car)**	**K, Th, U**	**Irregular grid**
Gamma-ray megacrystic	**Megacrystic granite**	**10 m**	**66.0 m**	**18.86 km2**	**Gamma-ray, dynamic mode (car)**	**K, Th, U**	**Irregular grid**
Eagle Regional	**Eagle High outcrops**	**0.5 m**	**7.2 m**	**0.43 km2**	**Gamma-ray, dynamic mode (foot)**	**K, Th, U**	**Irregular grid**
Eagle High	**Eagle high grid** *(near -26.0980, 30.6290)*	**0.5 m**	**1.22 m**	**1291.9 m2**	**Gamma-ray, dynamic mode (foot)**	**K, Th, U**	**Semi-regular grid**
River dynamic mode	**River outcrop** *(near -26.1722, 30.4434)*	**0.5 m**	**0.5 m**	**100 m2**	**Gamma-ray, dynamic mode (foot)**	**K, Th, U**	**Irregular grid**
River static mode	**River outcrop** *(near -26.1722, 30.4434)*	**0.5 m**	**1 m**	**100 m2**	**Gamma-ray, static mode (30s)**	**K, Th, U**	**Regular grid**

Steep dynamic mode	**Steep outcrop** *(near -26.1329, 30.4989)*	**0.5 m**	**0.4 m**	**56 m2**	**Gamma-ray, dynamic mode (foot)**	**K, Th, U**	**Irregular grid**
Steep static mode	**Steep outcrop** *(near -26.1329, 30.4989)*	**0.5 m**	**1 m**	**56 m2**	**Gamma-ray, static mode (3 x 30 s)**	**K, Th, U**	**Regular grid**
BO-12-07_1	**Boesmanskop** *(-26.0796, 30.7402)*	**0.1 mm**	**0.1 mm**	**1038 mm2**	**Autoradiography**	**U**	**Image 246x422 pixels**
BO-12-07_2	**Boesmanskop***(-26.0796, 30.7402)*	**0.1 mm**	**0.1 mm**	**1162 mm2**	**Autoradiography**	**U**	**Image 256x454 pixels**
HE-11-22A	**Heerenveen** *(Steep outcrop, -26.1329, 30.499)*	**0.1 mm**	**0.1 mm**	**1420 mm2**	**Autoradiography**	**U**	**Image 306x464 pixels**
MP-12-01_1	**Mpuluzi** *(Eagle High, -26.0957, 30.6297)*	**0.1 mm**	**0.1 mm**	**1258 mm2**	**Autoradiography**	**U**	**Image 282x446 pixels**
MP-12-01_2	**Mpuluzi** *(Eagle High, -26.0957, 30.6297)*	**0.1 mm**	**0.1 mm**	**833.6 mm2**	**Autoradiography**	**U**	**Image 242x396 pixels**
SEM_Poitiers	**Seven samples**	**10 microns**	**10 microns**	**600 mm2**	**SEM (Poitiers)**	**Si, Al, K, Na, Ca, P, Ti, Fe, Mg, Ce, La, Y, Zr, Th, U**	**Image 2000*3000 pixels**
SEM_LMV	**Seven samples**	**0.36 microns**	**0.36 microns**	**0.0972 mm2**	**SEM (Clermont)**	**Si, Al, K, Na, Ca, P, Ti, Fe, Mg, Ce, La, Y, Zr, Th, U**	**Image 1000*750 pixels**

Table 4. Summary of the dataset acquired (or compiled) in this study. Longitude/latitude coordinates are precise to ca. 20 m and are given for reference only.

575

The methods described above allows to assemble and analyse several datasets, and to describe chemical diversity of the Heerenveen Batholith at scales from ca. 10 km to < 1 mm (i.e. over 7 orders of magnitude) (Table 4 and Figure 5).

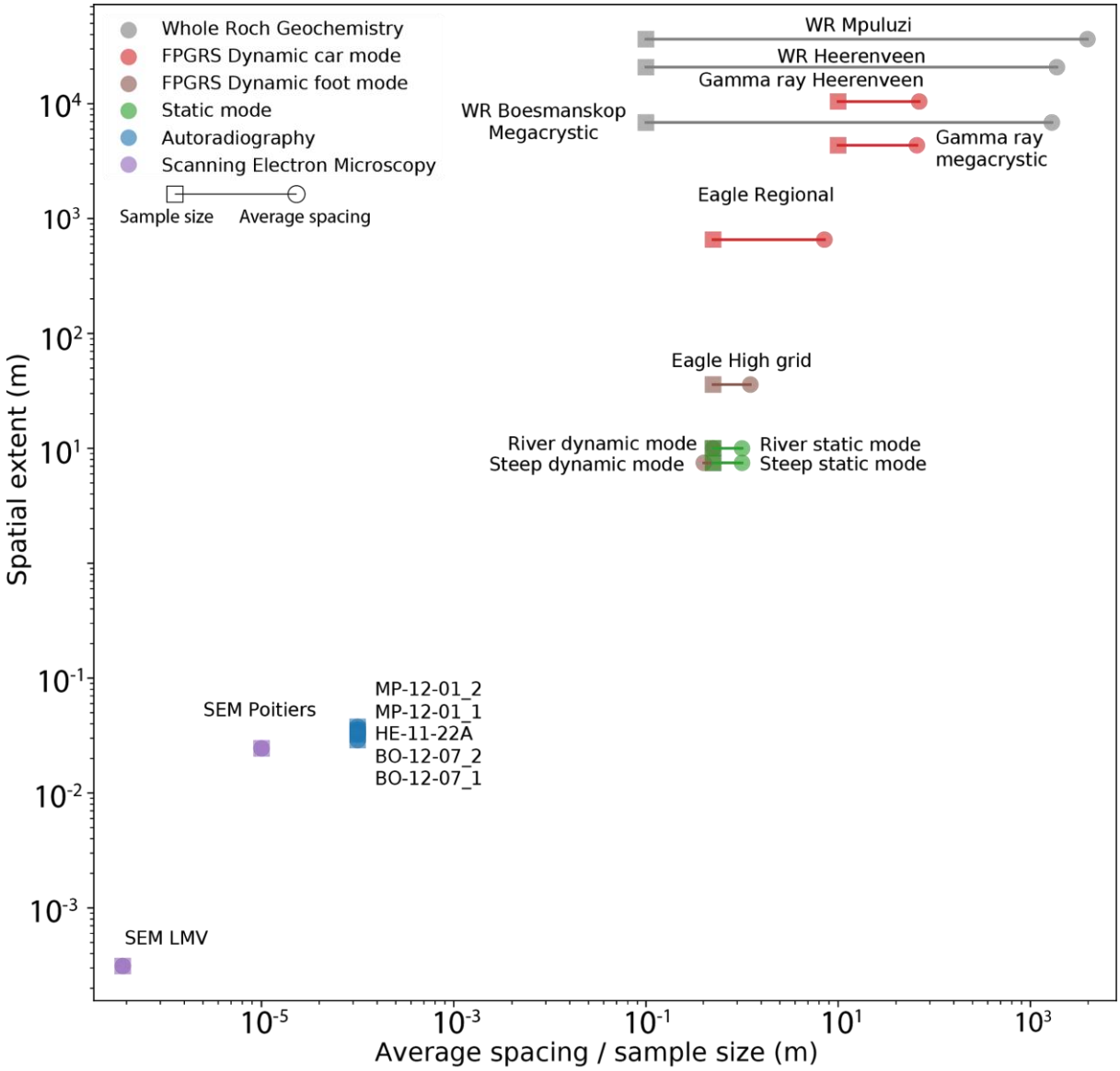

Figure 5. Summary of the datasets used in this work. For each dataset, we represent the extent (y-axis) and characteristic scales (x-axis) for sample size and sample spacing.

4.1 Batholith-scale datasets

At the scale of the whole batholith (up to 40 km), we use two distinct datasets. The first is the "conventional" type of geochemical dataset, i.e. geo-referenced whole-rock analyses. They suffer from many flaws, and for the scope of this study, the lack of representativity is an obvious one: samples were taken by geologists with specific purposes in mind. They were collected from outcropping portions of the batholith, and from places where it is physically possible to sample. As commonly observed in such studies, geologists tend to undersample the "boring",

dominant representative phase at the expense of the more "interesting", unusual rock types. These limitations will be highlighted in the statistical analyses presented here. We have three such datasets available (Appendix EA1), one for whole-rock analysis from the Heerenveen batholith, a subset of the first focussing only on the core *megacrystic granite*, and one for the Mpuluzi batholith.

Similarly, we performed targeted gamma-ray measurements on selected rock types, with a strategy similar to conventional sampling – i.e. describe the properties of rock types identified a priori. This dataset is not amenable to spatial treatment.

To alleviate the biases inherent to rock sampling, we explore the use of gamma-ray mapping. In the Southern portion of the Heerenveen (up to 20 km), we assembled a "car mode" gamma-ray dataset, for U, Th and K. Although less accurate, this dataset is more representative and allows more regular "sampling". This dataset includes > 22500 data points. About 120 km^2 are covered, for which no point is further than 2 km from an actual measurement. A subset with 4450 points was extracted from the portion that covers only the main *megacrystic granite*. Both datasets are available in Electronic Appendix EA3.

4.2 Outcrop-scale datasets

At a scale of a few tens to hundreds of meters, we assembled outcrop-scale gamma-ray maps. The chain of outcrops at Eagle High was surveyed using "dynamic foot mode". Although this dataset is of lower quality compared to the others (no systematic pattern, alternating sectors with excellent outcrop and thick soil), it nevertheless fills a gap and supplies the only information that we have at a ca. 1 km scale. The information here covers 0.6 km^2, with 8500 measurements, and is also reported in Electronic Appendix EA3.

For the two selected outcrops that were mapped in detail in the Heerenveen batholith, we have both a "dynamic foot mode" and a "static mode" grid. The trade-off is that the "dynamic" grids have lower accuracy, but the increased spatial density is more amenable to spatial statistics. In the "river" locality, the static grid includes 122 data points, whereas the dynamic grid has more than 450 measurements (73 and 370 for the "steep" locality). We also acquired a dynamic mode grid (> 900 data points) at Eagle High, in the Mpuluzi batholith, but no static mode grid. All these data are given in Electronic Appendix EA3.

In addition, on the outcrops mapped in detail, we also acquired a series of "static" gamma-ray measurements, without a spatial framework but focussing on individual rock types, with the aim of characterising the gamma responses of individual rock types.

4.3 Thin section-scale datasets

Autoradiography was performed on several cm-sized fragments of five samples, offering at least a qualitative view of the U distribution at a scale of a centimetre. The alpha count images as well as underlying SEM images are supplied as Electronic Appendix EA4.

Lastly, SEM maps and images provide information on a mm-scale. These data are therefore much less amenable to statistical treatment and are not used for this purpose here.

5. Where is U in the Heerenveen batholith?

Our datasets, having been assembled with spatial information in mind, are particularly amenable to this treatment, and we start by investigating the spatial distribution of elements (U in particular) in the batholith.

5.1 Elements distribution at the batholith scale

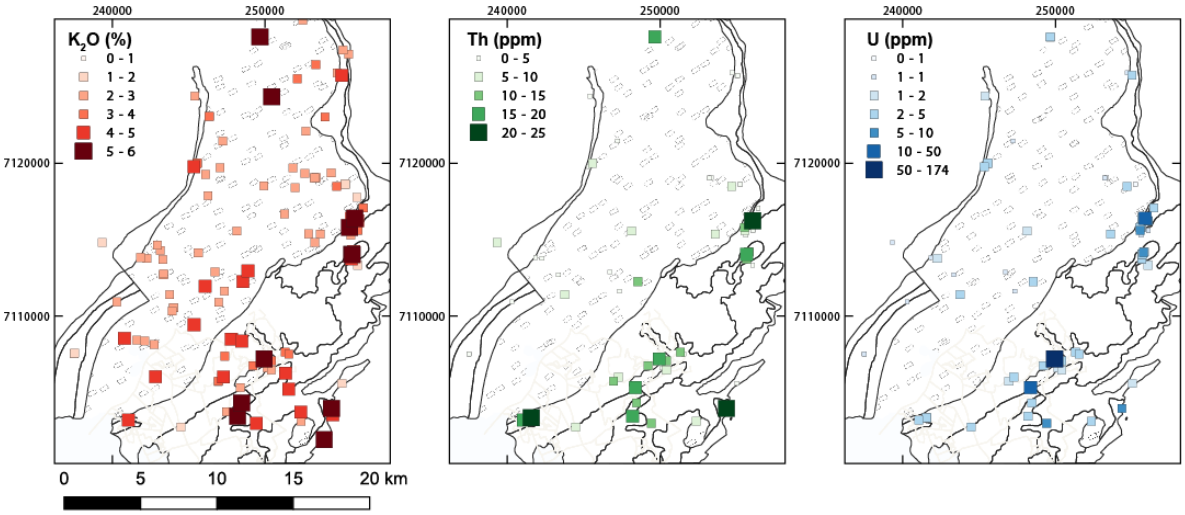

Figure 6. Concentrations of U, Th and K in analysed whole-rock samples, on the outline geological map (Figure 2). The pattern filled with rectangles corresponds to the *megacrystic granite* and the other map units are left blank.

Whole rock geochemical and spectrometric analyses showed that the core of the Heerenveen Batholith, made of a homogeneous GMS *megacrystic granite* intrusion, has relatively low Th and U contents, similar to those of the TTG country rocks. In contrast, the most enriched samples are essentially found in the late phases associated with the marginal shear zones.

Most of the late intrusions are enriched in both Th and U, with a Th/U ratio around 3 to 4 that prevent the crystallization of uraninite. Only the second generation of leucogranites and some pegmatite dykes or units closely associated with them, are sufficiently enriched in U, relative to Th, to permit uraninite crystallisation. Those U-enriched dykes are different in the two batholiths. In the Mpuluzi batholith border they are late, undeformed sub-horizontal pegmatite dykes that cut accross all other rock units, whereas in the Heerenveen batholith they are associated with the *leucogranite 2*, emplaced before the last intrusive phases, and are more or less intensively deformed in the shear zone. Due to the ductile deformation and the fracturing, U has been locally remobilised by hydrothermal fluids that have circulated within the shear zone, especially in the Heerenveen Batholith.

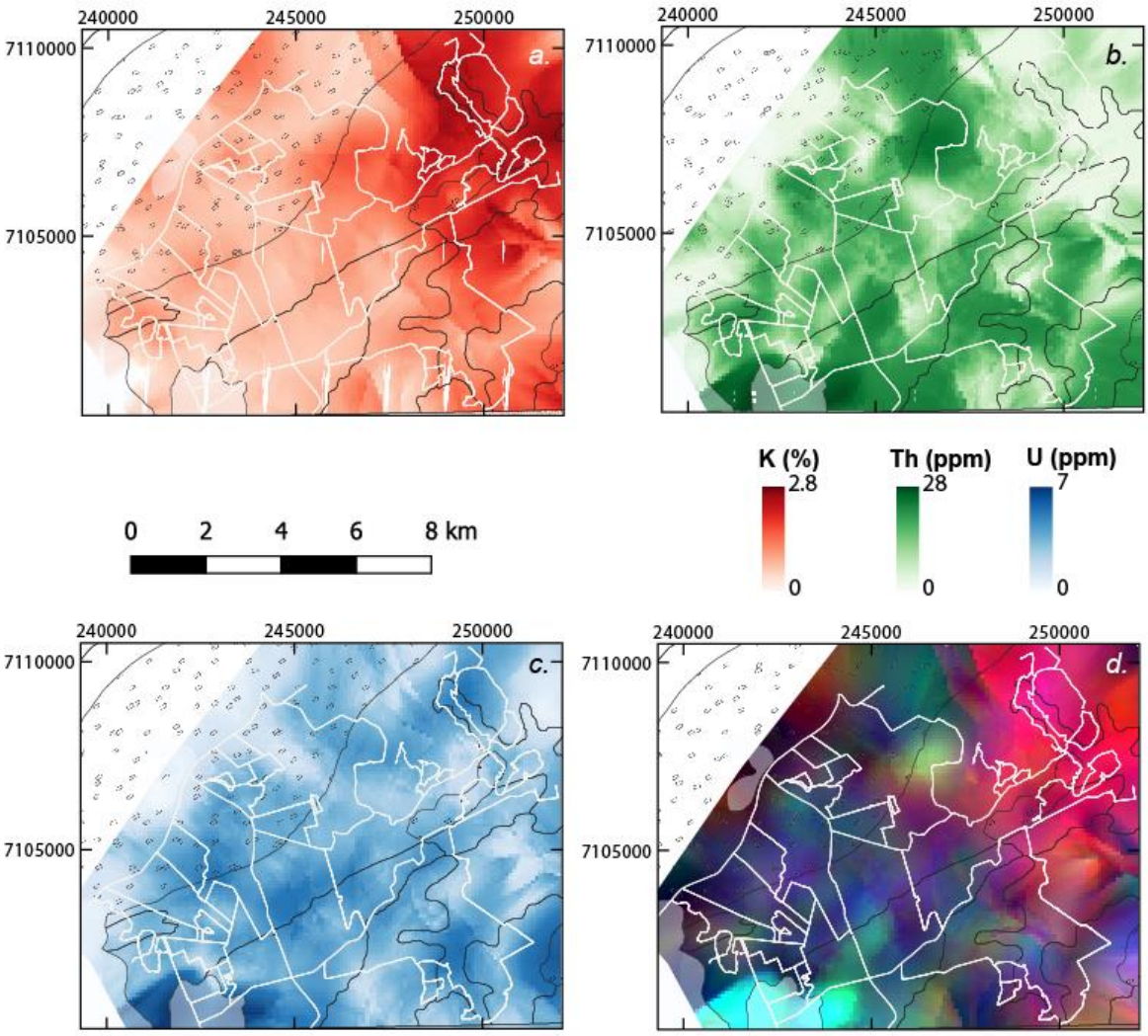

665

Figure 7. Batholith-scale interpolated maps for K (a, red), Th (b, green) and U (c, blue), from gamma-ray data (see scale bar for color-codes of concentrations). (d). RGB composite K-Th-U image with K mapped to the red channel Th to the green channel and U to the blue channel. Map extent and outline of geology are from Figure 2, rectangle pattern shows the *megacrystic granite*. The white lines correspond to the acquisition
670 **tracks, made of a large number (> 22500) of individual measurements used for interpolation.**

The batholith-scale gamma-ray dataset supplements the information from rock samples. The core of the batholith (the *megacrystic granite*) has a low radioactive element background (< 2.5 ppm U, with a mean U content of 1.3 ppm; mostly < 3 % K_2O and < 5 ppm Th). However, the
675 interpolated maps (Figure 7) suggest that, within this overall domain of low concentration, the actual distribution is rather patchy, in particular for U and Th (as observed in the variographic analysis). This is less true for K_2O. Furthermore, the patches are spatially uncorrelated (Figure 7), resulting in domains with contrasting K/Th/U ratios in the core of the Heerenveen batholith (strong colour variations in Figure 7d).

Incompatible elements (in particular U) are concentrated preferentially within the marginal shear zones and/or within the late intrusive phases associated with these shear zones. The East border shear zone contain up to 174 ppm U, from a sample selected with the spectrometer (mean at 3.6 ppm). However, the late intrusions (*quartz-monzonite, pink granites 1 & 2*) are typically enriched both in U and in Th, maintaining a primitive Th/U ratio of about 3-4 that did not permit uraninite crystallisation. Only some facies of *leucogranite 2* (forming patches too small to be mapped in Figure 7) show significant U—Th decoupling.

In the Mpuluzi Batholith, no regional gamma-ray map is available, but the border shear zone also contains the samples with some of the highest U levels (up to 400 ppm, mean at 5.2 ppm). Here again, the main phase appears to have moderate levels of incompatible elements (U < 2 ppm, average Th 9 ppm, average K_2O 2.8 %), compared to the marginal phases (median U 4.3 ppm, average Th 17 ppm, average K_2O 4.1 %). U/Th fractionation is again moderate, except in late pegmatites.

5.2 Elements distribution at the outcrop scale

The three outcrops investigated in more details are all in the enriched border zones of the Heerenveen (River, Steep) and Mpuluzi (Eagle High) batholiths.

5.2.1 The “river” outcrop

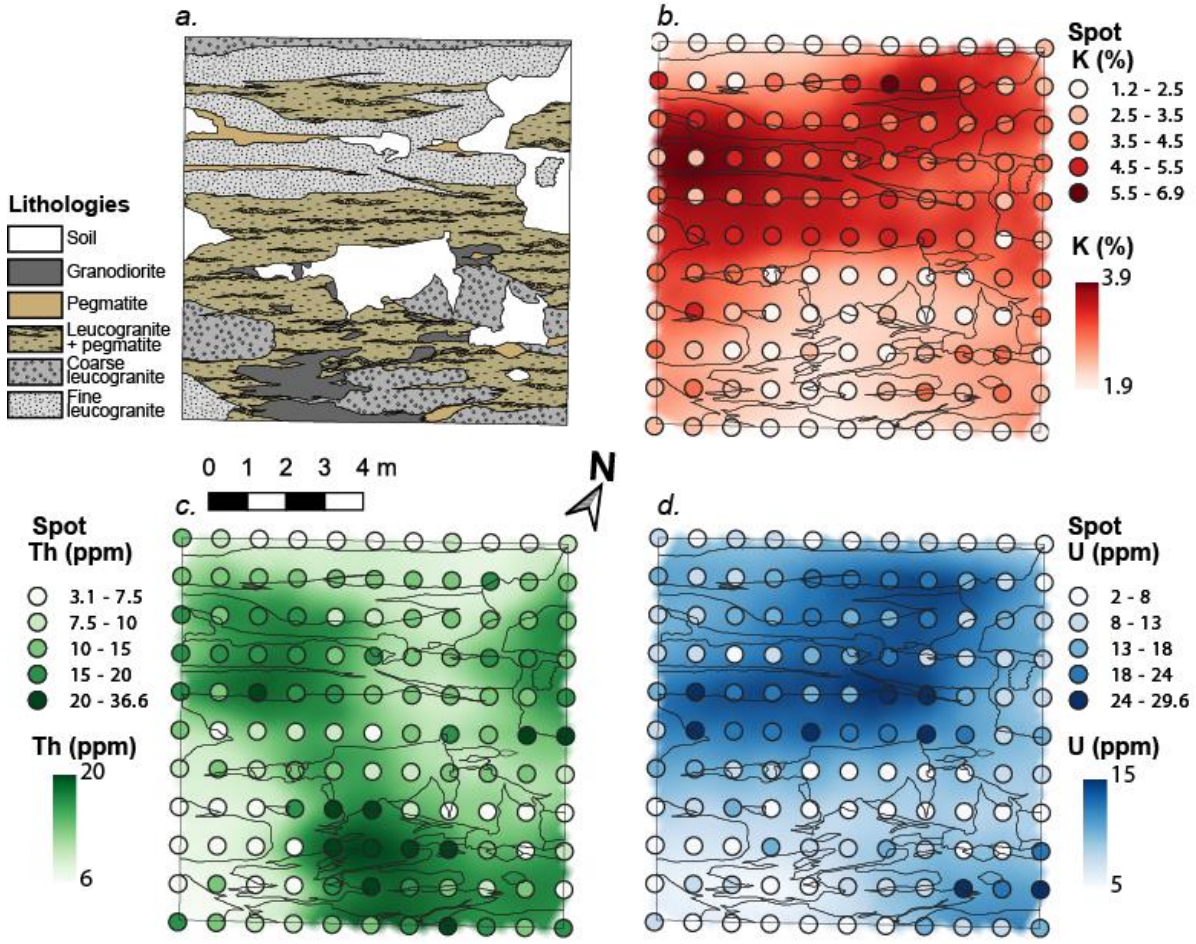

Figure 8. Lithological (a) and gamma-ray (b—d) maps for the “River” outcrop. For each composition map, both the spot analyses (circles) and the interpolated grid (background) are depicted.

The “river” outcrop consists of several phases of leucogranites (all belonging to *leucogranite 2*) injected into an active shear zone (Figure 8; Figure 3c and d), with some pegmatite and granodiorite dykes. The various batches of leucogranite apparently intruded the shear zone at different times during its activity, and range from strongly deformed (early “fine-grained” leucogranite) to nearly undeformed, (latter “coarse-grained” leucogranite). The pegmatite dykes are boudinaged or even stretched and dismembered in the leucogranite (Figure 3c). Aligned K-feldspars deriving from a nearby pegmatite are visible in the early leucogranite sheets, but not in the late, coarse leucogranite (Figure 3d).

High K values correlate with the “fine-grained leucogranite” (Figure 8) and its pegmatites. The other phases have lower K contents. Once again, U and Th form a different pattern. Whereas high values are exclusively found in the pegmatite-rich portions of the leucogranite, the

distribution is random, with high concentration patches neighbouring lower concentration domains. Th/U ratios are also variable; the three highest U contents (29, 27 and 27 ppm) are associated with moderate Th contents of 6, 6 and 15 ppm, and correspondingly low (0.2 – 0.5) Th/U ratios. In contrast, the highest Th spots (three spots at 36 ppm) have moderate U contents (15, 8 and 15 ppm) and moderate (2, 4 and 2) Th/U ratios. This is related to fluid/melt fractionation, with fluid expelled from the pegmatites/aplites. As discussed above, since gamma-ray spectrometry integrates the contributions from a ca. 1 m^3 volume of rocks, likely the "true" concentrations of U-rich 10 cm-sized samples (typical hand specimen) in this outcrop are much higher, although this is, of course, impossible to evaluate without further spatial information at the sub-meter scale.

5.2.2 The "steep" outcrop

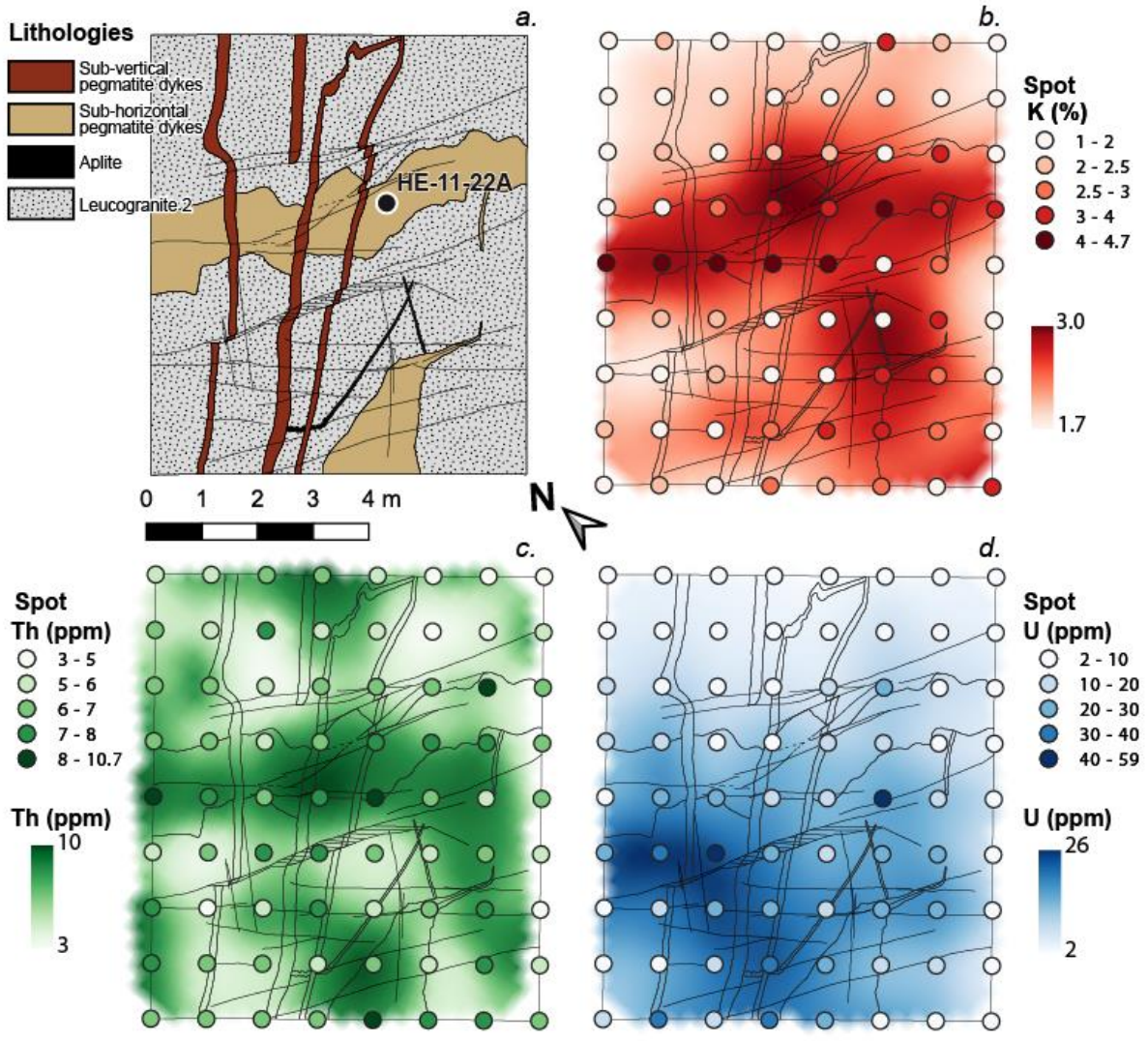

Figure 9. Lithological (a) and gamma-ray (b—d) maps for the « Steep » outcrop. For each composition map, both the spot analyses (circles) and the interpolated grid (background) are depicted. The location of sample HE-12-22A, studied for autoradiography, is indicated.

The "steep" outcrop shows the same rock units as the "river" outcrop, except that these rocks are less deformed. The main phase of this locality is the leucogranite 2, here cut by two sets of pegmatites: an early set of sub-horizontal pegmatites, and a latter set of NE—SW trending (i.e. the direction of the shear zone) narrow vertical pegmatites, with sharp contacts with the granite (Figure 9).

The highest K contents are here associated directly with the (horizontal) pegmatite, whose width generates a clear signal. U and Th are patchy and uncorrelated. We postulate that U (and Th) hotspots are related to the network of fractures, with chlorite-illite infilling, that cut the outcrop. As the fractures either displace or are cut by the pegmatites, they belong to the same event, and their mineral infilling probably precipitated from pegmatite-related fluids. Immediately East of the mapped grid, sample HE-12-01 (identified by gamma-ray survey) was found to contain 174 ppm U and only 3 ppm Th (Th/U = 0.017) in whole rock analysis (ca. 40 ppm U in gamma-ray).

5.2.3 The Eagle High outcrop (Mpuluzi)

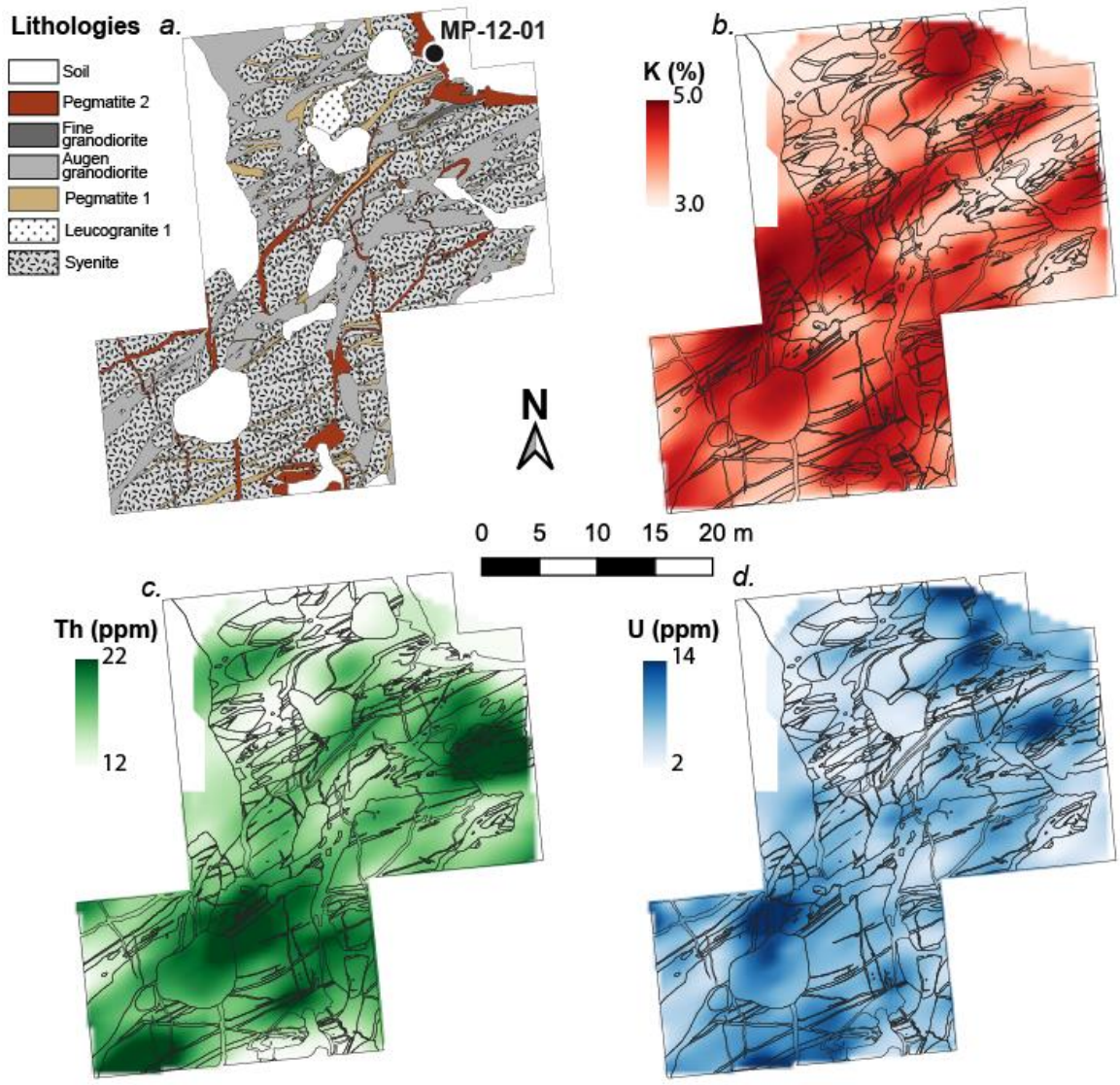

Figure 10. Lithological (a) and gamma-ray (b—d) maps for the "Eagle High" outcrop. Only the interpolated grids are shown for each element. The location of sample MP-12-01, studied for autoradiography, is indicated.

A lithological map for the "Eagle High" outcrop is presented in Figure 10, and illustrated by field photographs Figure 3(e-f). The main feature is a magmatic breccia, with large (metre-sized) fragments of syenite wrapped in a dark, *augen granodiorite* matrix. Numerous pegmatites, belonging to different sets, cut the various components. This very large outcrop also features 5 m-wide pegmatite dykes, equivalent to the mapped *pegmatite 2* that were not included in the detailed mapping due to their size (the edge of one of those appears in the NE corner of our detailed map, Figure 10).

Although the correlation is not very good, the K map shows an anisotropy mimicking the dominant structural grain in the outcrop (i.e. that of the Weltverdiend Shear Zone). High K contents correlates with the syenites, whereas low K is found in the granodiorite that makes up the matrix of the breccia. Once more, the U and Th contents are patchy and uncorrelated. High U, in particular, tends to be associated with the largest *pegmatite 2* (e.g. in the NE corner of the map area). The highest concentration in this outcrop, sample MP-12-01, was found in a 3 m wide *pegmatite 2* dyke immediately outside of the mapped area, with 400 ppm U, 91 ppm Th (Th/U: 0.22) and 1.27 % K_2O in hand specimen.

5.3 Uranium distribution at the thin section scale

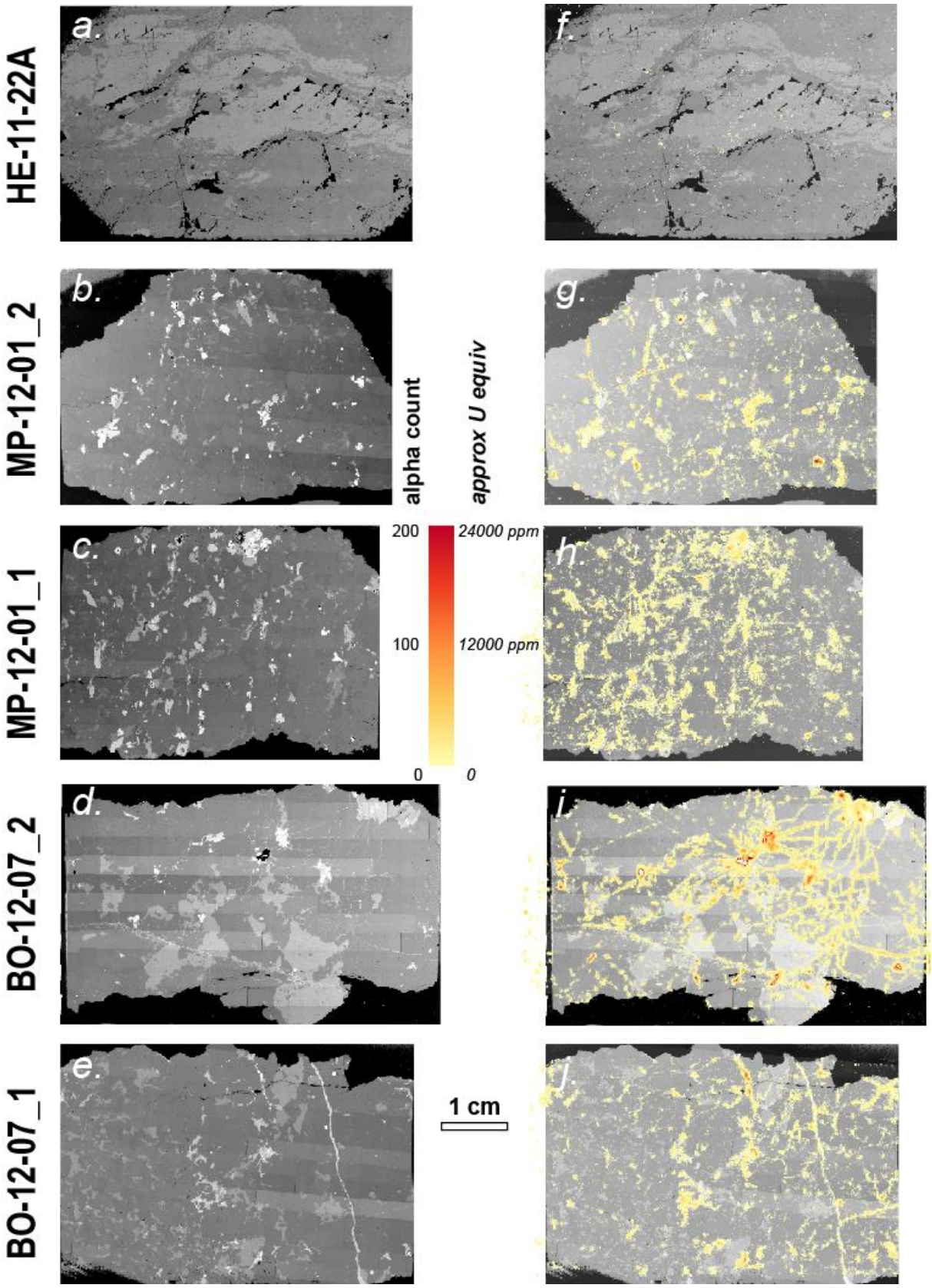

Figure 11. SEM images (a—e) and SEM images, with alpha count map superposed (f—j), for the 5 samples mapped by BeaQuant autoradiography. Scale and colour codes are the same in all images. The conversion of counts to ppm is approximate (see text).

Three samples (Fig. 11) mapped using alpha autoradiography allow to discuss U distribution.

In the U-poor (5.9 ppm) sample HE-11-22A, U is scattered at a sub-pixel (i.e. < 100 µm) scale, forming very small grains of U-rich phases with no further control. The distribution appears to be essentially random (Figure 11a and f).

The autoradiographies in the thin sections from sample MP-12-01 (large *pegmatite 2* at "Eagle High") reveals small to medium radioactive spots scattered throughout the thin sections, and less common larger spots clustered in some parts of the sample (Figure 11b-c and g-h). Groups of small, aligned, highly radioactive spots suggest deposition of uraninite crystals along submagmatic fractures.

Sample BO-12-07 is taken from the Weergevonden "tail" *syenogranite* intrusion (Figure 11d-e and i-j). The Boesmanskop/Weergevonden complex is made of syenites and syenogranites, emplaced at about the same time as the Heerenveen and Mpuluzi batholiths. These units are correlated with the syenogranite phase encountered at the "Eagle High" outcrop situated in the northern part of Mpuluzi margin, close to the Boesmanskop/Weergevonden complex. This sample is from a pegmatite dyke, showing a dense fracture network filled with a fine yellowish to greenish material corresponding to uranophane $Ca(UO_2)_2(SiO_3OH)_2 \cdot 5H_2O$. The whole rock contains 588 ppm of U, for 162 ppm of Th and a Th/U ratio of 0.28 similar to the one of the pegmatite from the Eagle High zone. Autoradiographies in two sections from sample BO-12-07 reveal some small to large radioactive spots, but also selective distribution of the radioactive material along a fracture network that radiates around the most radioactive spots and locally joins several intensively radioactive spots. Such a distribution suggests redistribution of U from the easily leachable uraninite (strong radioactive spots) into fractures as hexavalent uranium minerals during infiltration of oxidizing meteoric waters.

6. How is U concentrated and fractionated in the Heerenveen batholith?

6.1 U enrichment and fractionation

Binary plots are common tools used to display variations and inter-relations between small numbers of variables, and the interpretation of "trends" is at the core of geochemical reasoning. The Heerenveen Batholith is no exception, and we can use this approach to constrain the processes responsible for its chemical evolution. Here, we propose a series of fractionation mechanisms that can explain the different types of radioelement enrichment revealed in the Mpuluzi, Heerenveen and Boesmanskop intrusions. They are best expressed in log(Th) vs. log(U) diagrams (Figure 12; Figure 13)

First, we note that qualitatively, the whole-rock analyses and the gamma-ray "facies orientated" analyses depict similar patterns (Figure 12). For practical reasons, pegmatites were not sampled for whole rock analysis because large grain size would have required large samples, which would have been impossible to extract from the flat outcrop surfaces typical from the area. Pegmatites are thus nearly absent from the whole-rock dataset, and, in that sense, the gamma-ray data nicely complement the conventional geochemical observations. On the other hand, the absolute values of K, U and Th differ between the gamma and whole-rock measurements, for the reasons discussed in section 3.2.

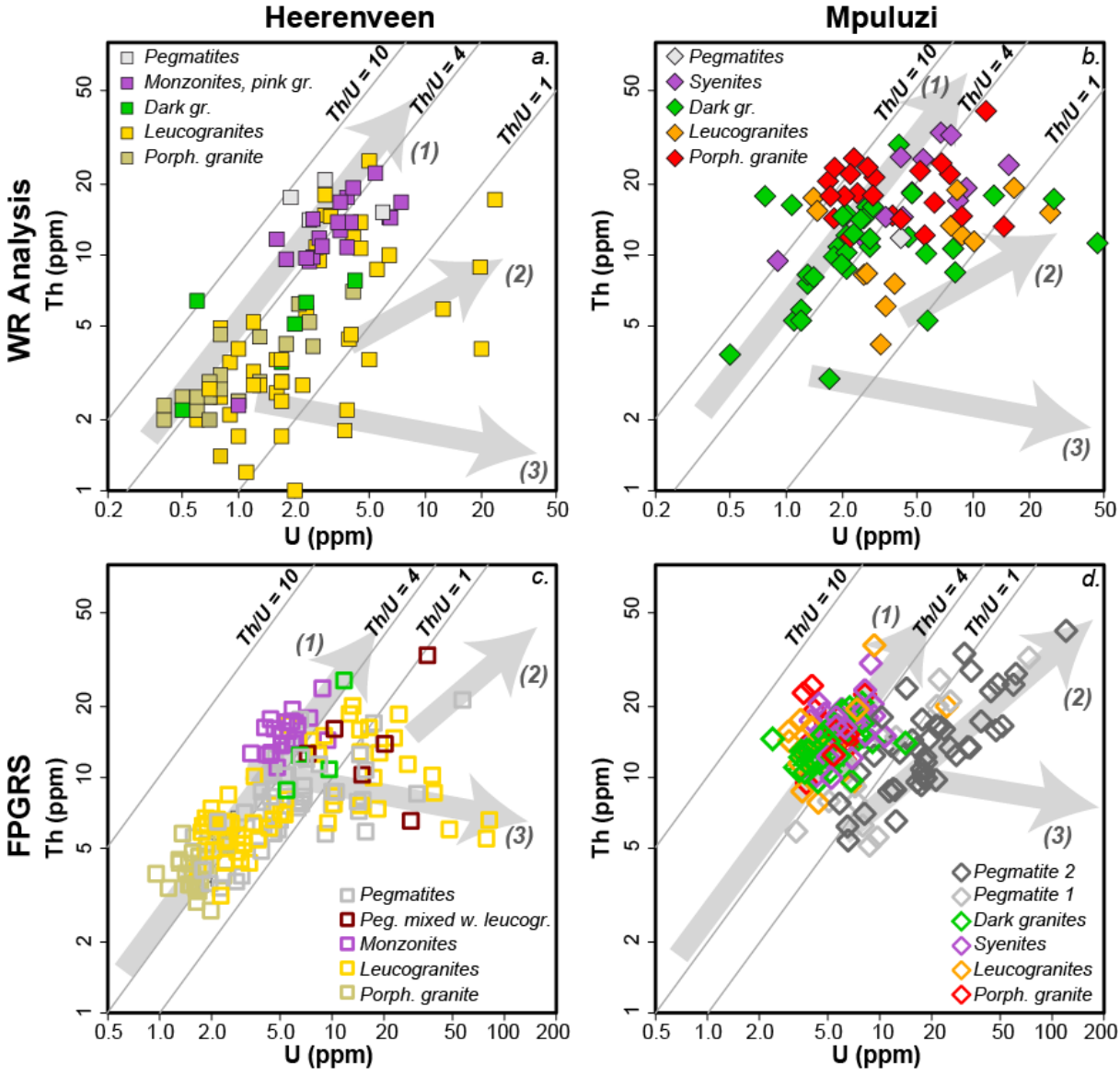

Figure 12. log(Th) vs log(U) binary plots for (a—b) whole-rock analyses and (c—d) spot, facies-oriented gamma-ray measurements of (a, c) the Heerenveen and (b, d) Mpuluzi batholiths. Arrows labelled 1—3 correspond to the three enrichment processes discussed in the text.

Most of the granites of the Mpuluzi and Heerenveen batholiths present simultaneous enrichment in Th and U, with a relatively constant Th/U typical of magmatic fractional crystallization in moderately uranium-rich metaluminous melts (Cuney, 2014). However, the Th/U ratios vary extensively (from about 1 to more than 4), which may reflect some U mobility due to exsolution of late magmatic fluids from crystallising melts and the later percolation of oxidizeing meteoric waters in the surface samples. This interpretation is supported by the shift towards higher average Th/U ratios in the Th-richest samples, where uranium can be hosted in accessory minerals (uraninite, metamict uranothorite or allanite) from which uranium can be more easily leached by meteoric waters, compared to samples with low Th and U contents

where uranium is mostly hosted in more refractory phases such as zircon, monazite and apatite. The enrichment for these samples reaches about 30 ppm Th, which would correspond to 7.5 to 15 ppm U for an initial Th/U ratio of 4 to 2. Such U and Th enrichment and Th/U lead to the crystallization of uranothorite or allanite in metaluminous high-Ca magmas or to monazite in peraluminous low-Ca magmas (Cuney and Friedrich, 1987), but do not permit the crystallization of significant proportions of uraninite.

A second type of U and Th fractionation is revealed by the trend showing simultaneous enrichment of these elements with lower Th/U ratios in the Mpuluzi pegmatites (Figure 12), with decreasing Th/U ratios from about 1 to less than 0.3. This trend may reflect two processes: (i) preferential fractionation of a mineral with high Th/U (such as monazite) with increasing peraluminosity of the melt and decreasing temperature during fractionation, (both parameters decrease monazite solubility; e.g. Montel, 1993) (Fig. 12d); (2) late magmatic uraninite enrichment crystallizing from magmatic fluids in submagmatic fractures (Bouchez et al 1992) as suggested by the alignment of small uraninite crystals on the autoradiography, and the larger crystals may correspond to primary uraninite crystallised directly from the magma (Fig. 11). Such bimodal distribution of uraninite was previously described in the Rössing pegmatoids ("alaskites") in Namibia (Cuney and Kyser, 2009) or the St Sylvestre granite in the French Limousin (Cuney et al., 1990).

A third type of U and Th fractionation is observed in the Heerenveen *leucogranite 2*, with U enrichment without concomitant Th enrichment, or even a slight decrease in Th concentrations (Figure 12). Such a trend is clearly related to the remobilisation of U, with Th being sparingly soluble in medium- to low-temperature fluids. The U enrichment being related to brittle fractures and U being associated dominantly with Ti-oxides further confirm the hydrothermal to supergene origin of this type of fractionation.

In "global" datasets (Figure 13, a and b), some data points also correspond to sharp U depletion at constant Th (trend 4), which is due to weathering and preferential U loss. This is not visible in smaller-scale datasets, that were acquired on fresh surfaces, purposely avoiding alteration zones.

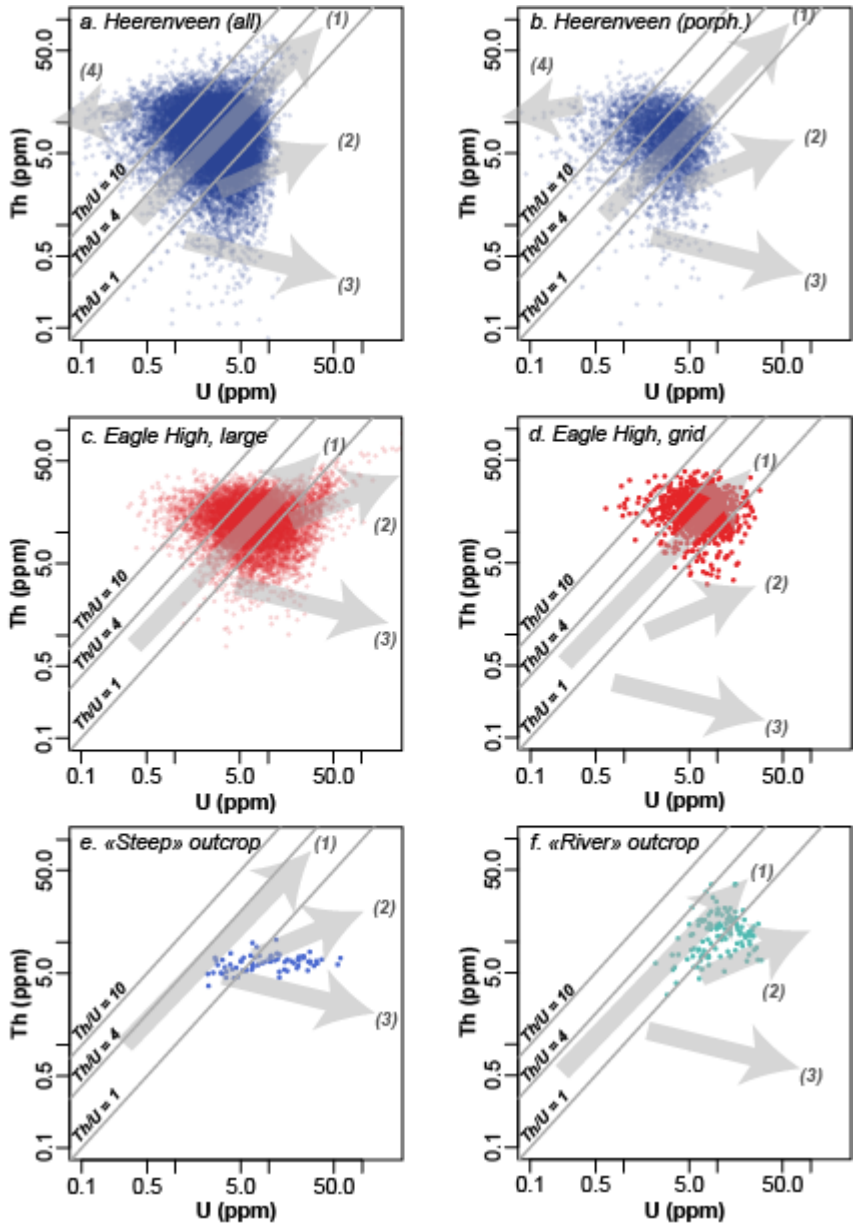

Figure 13. Log(Th) vs log(U) binary plots using batholith-scale (a—b) or outcrop scale (c—f) gamma-ray datasets. Although the absolute values differ from sample-based data (Figure 12), the qualitative patterns are similar. Arrows labelled 1—4 correspond to the processes discussed in the text (1 = magmatic fractional crystallization in moderately uranium-rich metaluminous melts, 2 = magmatic fractional crystallization and addition of uranium by infiltration of magmatic fluids or late melts, 3 = hydrothermal to supergene remobilisation of U, 4 = weathering).

The spatially-controlled gamma-ray datasets, at batholith-scale as well as outcrop-scale, depict similar patterns (Figure 13). The full Heerenveen dataset, as well as the dataset restricted to the core megacrystic facies (Figure 13 a and b, respectively), define relatively dense clusters. A weak evolution towards higher U and Th (trend 1) is observed for the full dataset (Figure 13a) but is not apparent in the dataset restricted to a single facies (Figure 13b). This is in line with

our conclusions from conventional, sample-based interpretations. The trends towards high U with U/Th decoupling (trends 2 and 3) are hardly or not at all visible in either dataset. This is expected from the core dataset (as this process occurs mostly in the marginal shear zones of the batholith) but less so in the full dataset. This suggests that these processes are volumetrically minor, a fact obscured by the "cherry-picking" inherent in sampling. A tail towards low Th (and constant U) does not match any of the processes we identified and we speculatively relate it to fractionation during alteration, transport and accumulation in the regolith.

The two "Eagle High" grids show essentially similar patterns (Figure 13 c and d). In the "large" grid, a small group of points defines a trend similar to our trend (2), identified, in the same outcrop, on the basis of sampling.

Finally, the two small-scale grids ("steep" and "river") display more interesting properties. In the "steep" outcrop in particular (Figure 13 e), a clear subhorizontal trend (trend 3) is clearly visible and dominant. The "river" outcrop (Figure 13 f) is less clear, but could be read as a combination of trends 1 and 2.

Collectively, the gamma-ray spatially controlled grids show evidence for a superposition of processes. On small outcrops, admittedly chosen to reveal a specific process, the selected process is clearly visible. At larger scales, the resulting data appear to average many individual processes and this results in rather blurred patterns that are hard to deconvolve.

6.2 Mineralogical control

We conducted a survey of selected samples, to relate our findings on the controls of U distribution to mineral chemistry.

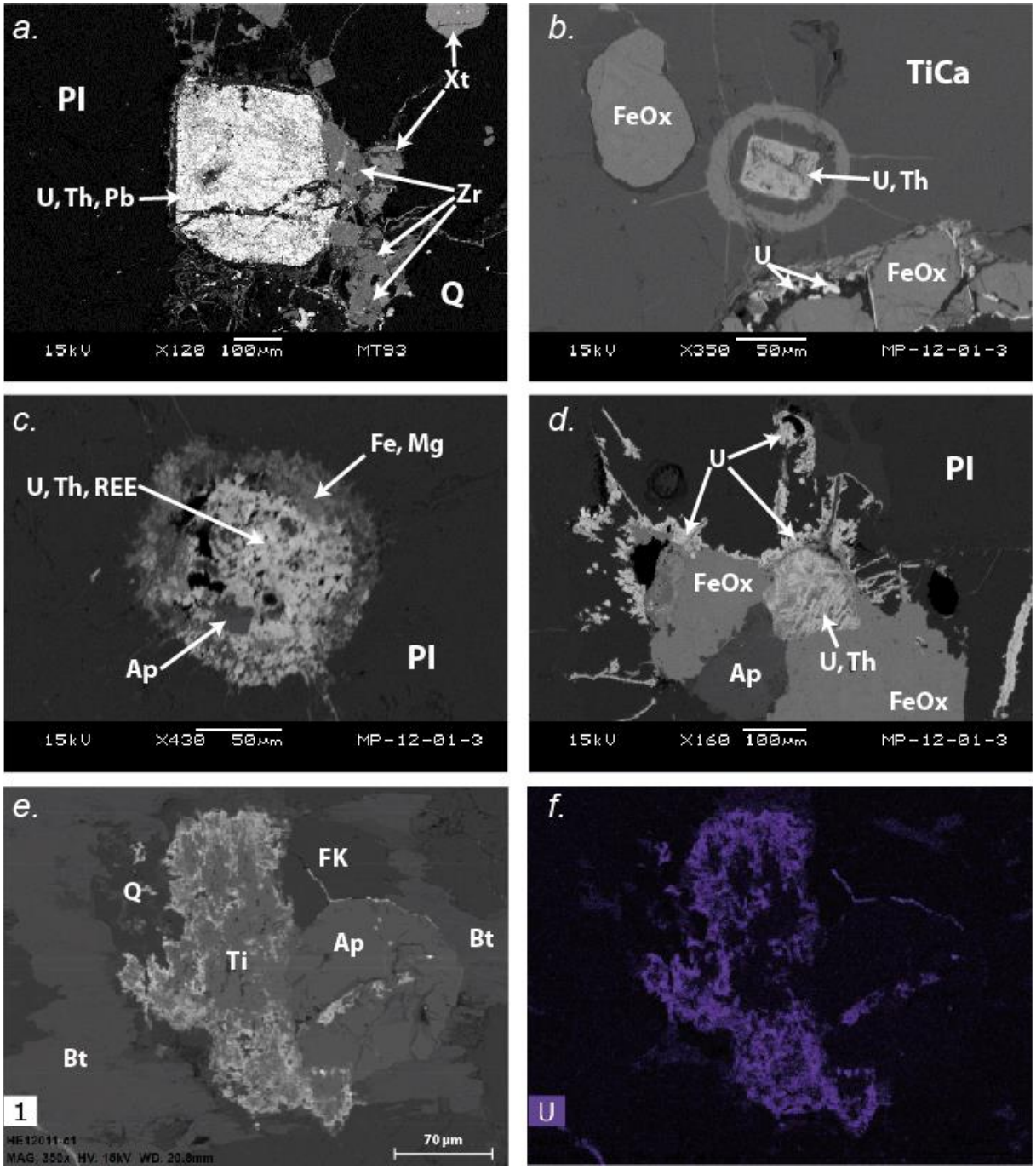

Figure 14. Partially altered uraninite crystals from the sample BO-12-07 (a) and MP-12-01 (b—f). (a—e): SEM backscattered images, (f): U abundance map, same field of view as (e). Mineral abbreviations: KF, K-Feldspar; Pl: Plagioclase; Bt: Biotite; Zrn: zircon; Xtm: xenotime; FeOx: iron oxides; Ttn : titanite; Ap : apatite; Urn: Uraninite.

Seven samples with up to 26 ppm U (whole-rock) were investigated under the SEM. Their U/Th, U/Nb, U/Zr and U/Y ratios are variable, and they offer an opportunity to investigate the large variety of accessory minerals that may incorporate U: thorite, monazite, xenotime, zircon,

Ta-Nb accessory minerals such as aeschynite-group, euxenite-group (Škoda and Novák, 2007) or betafite-group minerals (Lumpkin and Ewing, 1996). The U-richest thorite analysed is from the U-bearing conglomerates of the Witwatersrand Supergroup, and contains 30.51 wt.% UO_2 (Smits, 1989; Förster, 2006). Monazite shows a strong preference for Th over U, with Th/U ratios typically > 10, with rare exceptions (Förster, 1998). Experimental data show that, at 800 °C, uranothorite in equilibrium with uraninite contains 30 wt% UO_2 (Cuney and Friedrich, 1987). Consequently, U cannot be completely incorporated into thorite or monazite as long as the whole rock Th/U ratio is < 1. Likewise, xenotime can incorporate U up to 6.7 wt.% UO_2 (Förster 1998), and with a Y/U ratio of 7.5, U cannot be totally incorporated into this mineral. The U-richest granitoid zircons in the literature were analysed by Belousova et al. (2002) and include up to a few wt.% UO_2, 12 381 ppm U (Zr/U = 39.5). Förster (2006) analysed zircons containing up to 6.25 wt.% UO_2 (Zr/U at 8.34) and refers to the maximum U found in a zircon at 14.8 wt.% UO_2 (Zr/U = 3.12), but such concentrations are reached in local domains of the grain, and its average U concentrationis much lower.

The samples selected for our mineralogical study all have Th/U < 1 (except three relatively U-rich samples with Th/U between 1 and 3), Y/U < 5.5 and Zr/U < 38, so that they should contain U in excess to what can be accommodated in monazite, xenotime and zircon, and thus, uraninite may have crystallized.

A few tens of zircon crystals, about 10 to 200 μm in size, were found in each thin section, as well as several monazite crystals of 20 to 100 μm, and just one or two xenotime crystals in each thin section except in BO-12-07 in which xenotime is more common. Most monazite crystals are altered (except those enclosed in non-fractured quartz crystals) and partially or totally replaced by secondary apatite. REEs from the altered monazites are incorporated into newly formed allanite crystals that developed around them (Figure 14). Thorium stays in the site of former monazite crystals, to form small xenomorphic uranothorite grains, and also partly in the newly formed allanite crystals surrounded by apatite. Part of the uranium liberated during monazite alteration is incorporated into the uranothorite crystals, apatite and allanite, but part was probably released into the alteration fluids, as calculated by Negga et al. (1986). Except for the small, secondary uranothorite grains within the altered monazites, a few altered primary uranothorite crystals were observed in a sample with Th/U ratio < 1 (MP-11-12). Finally, strongly altered euhedral crystals of uraninite, with characteristic square sections, a radiation

damaged-halo in the enclosing mineral and radiating microfractures exist in the uranium richest samples (MP-12-01 and BO-12-07).

In most of the samples, zircon crystals are euhedral, elongated, zoned, and weakly enriched in U (52 to 1194 ppm U in zircons from five Mpuluzi Batholith samples, with mean at 328 ppm, and 45 to 4024 ppm of U in zircons from sixteen Heerenveen Batholith samples, mean at 565 ppm). Only in the uranium richest sample from the Eagle High outcrop do zircons show some peculiar characteristics: they are zoned with a BSE clear core and a darker rim, have inclusions of galena, are very metamict, and surrounded by radial fractures. These zircons must have been very U-rich, explaining their strongly metamict character, the radial fracture patterns around them (due to volume change during metamictisation and subsequent hydration of the mineral), and the presence of galena presumably of radiogenic origin. Only the outer rims seem to be metamict and contains galena inclusions, the inner core are better preserved and now contains higher concentrations of heavy elements than the outer rims.

In addition, in one of the U-rich samples away from the hotspots (MP-11-12, with 25.84 ppm U, 15.16 ppm Th), a 10 μm crystal with a composition close to brannerite $(U,REE,Th,Ca)(Ti,Fe)_2(O,OH)_6$, was observed. However, it may also correspond to an amorphous mixture of U and Ti oxides. U-enrichments have also been observed at the altered margins of titanium oxide minerals such as ilmenite, anatase and/or rutile. The preserved cores of those crystals contain no U, whereas U concentrations close to the altered zone may reach up to 5 wt % UO_2.

This Ti–U association is also predominant in the most U-rich sample from the Heerenveen Batholith (HE-12-01) with U coating the titanium oxide minerals; in this sample, no uraninite was found. This seems to confirm the mobilisation of U by fluids, and its adsorption on titanium oxides.

Primary magmatic uraninite crystals occur in the samples that are most enriched in U (from a late pegmatite dyke from the Mpuluzi shear zone and the Boesmankop tail). Those uraninite grains are about 40 to 100 μm across (up to 300 μm for one grain from the BO-12-07 sample). They have been strongly altered by supergene fluids, with a residual thorium-rich core (though some contain more U than Th).

The microscopic study of the samples confirms the observations made at the outcrop scale. At least three mechanisms of U enrichment over Th seem to have occurred: (i) a dominantly magmatic process for the Mpuluzi margin that explains the simultaneous U and Th enrichment

within the late pegmatite dykes dominantly occurring as uraninite and the Boesmanskop tail which has the same Th/U ratios and in which primary uraninite is also observed; (ii) a hydrothermal process occurring in the Heerenveen eastern shear-zone where U is strongly enriched without Th enrichment and where U seems to be adsorbed on Ti-rich minerals; (iii) supergene remobilisation of U by oxidizing meteoric fluids leading to the formation of secondary minerals with hexavalent uranium.

7. Statistical properties of element distributions: from univariate distributions to spatial analysis

In this section, we examine how the evolution described above is reflected in the statistical properties of the different datasets we have assembled.

7.1 Univariate statistics

Figure 15 shows a compilation of all the histograms for U, Th and K concentrations, for each dataset. Electronic Appendix EA6 includes more detailed versions, with individual histograms and statistics for each dataset.

The three elements considered have different statistical behaviour, independent of the scale of observation.

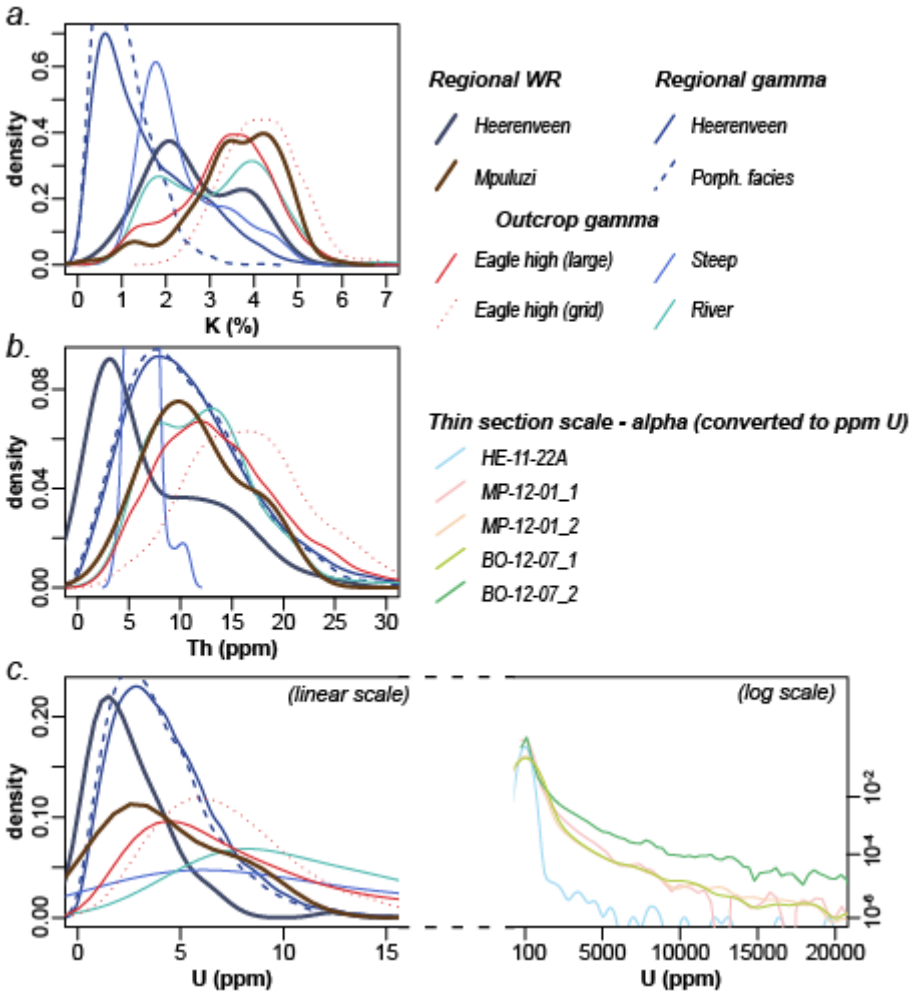

Figure 15. Univariate statistics: probability density distributions for the datasets considered for K (a), Th (b) and U (c). WR: Whole-rock.

	K					Th					U				
	Mean	St deviation	Rel. Sd	Skewness	Kurtosis	Mean	St deviation	Rel. Sd	Skewness	Kurtosis	Mean	St deviation	Rel. Sd	Skewness	Kurtosis
Gamma ray Heerenveen	1.16	0.81	70%	0.88	3.07	8.65	5.41	63%	2.18	14.39	3.27	1.98	60%	1.23	5.94
Gamma ray megacrystic	0.77	0.46	60%	0.99	4.10	8.04	4.40	55%	0.92	4.59	3.01	1.82	60%	1.04	4.39
WR Heerenveen	2.78	1.46	53%	2.51	13.71	7.52	5.87	78%	0.91	2.84	5.21	18.26	351%	8.75	81.15
WR Megacrystic	2.02	0.40	20%	-0.13	2.59	3.63	1.53	42%	0.78	2.40	1.34	0.98	73%	1.27	4.15
WR Mpuluzi	3.59	1.03	29%	-0.82	3.55	14.83	16.81	113%	4.09	19.14	21.69	80.74	372%	4.56	21.87
Eagle high all	3.34	1.08	32%	-0.27	2.78	14.01	6.57	47%	1.33	8.98	9.77	10.76	110%	8.21	144.37
Eagle high grid	4.17	0.83	20%	0.16	2.94	16.97	6.33	37%	0.54	3.38	7.52	3.87	52%	1.27	5.70
Steep spot	2.37	0.90	38%	1.03	2.92	6.41	1.18	18%	0.82	5.00	13.36	11.63	87%	1.70	6.39
River spot	3.18	1.17	37%	0.18	2.35	12.87	6.26	49%	1.55	6.51	12.19	6.36	52%	0.73	2.73
HE-11-22A											4.08	311.61	7644%	211.75	50198.65
MP-12-01_1											121.92	1205.89	989%	124.99	19229.12
MP-12-01_2											95.12	585.12	615%	24.29	928.92
BO-12-87_1											100.39	684.10	681%	42.90	3207.47
BO-12-87_2											301.60	1946.44	645%	40.32	2637.49

Table 5. Univariate statistic parameters for the datasets.

Potassium is nearly normally distributed (skewness close to 0, kurtosis close to 3) in datasets comprising a single facies (Heerenveen porphyritic whole rock), or dominated by one facies (Mpuluzi datasets). In composite datasets, the distribution becomes more skewed and generally retains a kurtosis close to 3. Although there are some outliers towards high values, they are not very prominent nor very far off these values. Visual inspection shows that, for datasets made

up of more than one rock type, the distribution curves tend to become bimodal, reflecting the different rock types. Thus, potassium appears primarily as a good indicator of rock types, as already described in conventional petrological studies (Clemens et al., 2010).

Uranium shows a markedly different pattern. All distributions are more or less positively skewed and have a high kurtosis, reflecting a large spread of values and frequent outliers. The whole-rock datasets have more dispersed distributions and higher standard deviations than gamma-ray datasets, presumably because of the larger scale of gamma-ray measurements, with respect to hand specimens, which are also occasionally selected for potential U enrichment (sampling bias). Large-scale datasets tend to be somewhat less scattered (lower relative standard deviations). The thin section scale datasets show extreme behaviour in this respect (and the distribution had to be represented using a log scale in Figure 15). Collectively, these features reflect the very uneven distribution of U that we demonstrated, with a very significant role for local (down to grain-scale) U accumulations even in rock that are otherwise U-poor.

The distribution of **Thorium** is intermediate between the previous two. It is more similar to K than to U, i.e. it appears to be correlated chiefly with rock types, with second-order variations related to the accumulation of Th-rich minerals. This reflects an important difference between the behaviours of the two trace elements. Whereas U occurs mostly in very small amounts of high-concentration, U-bearing phases, Th substitutes in a larger range of more common minerals (e.g. phosphates such as monazite).

7.2 Spatial analysis

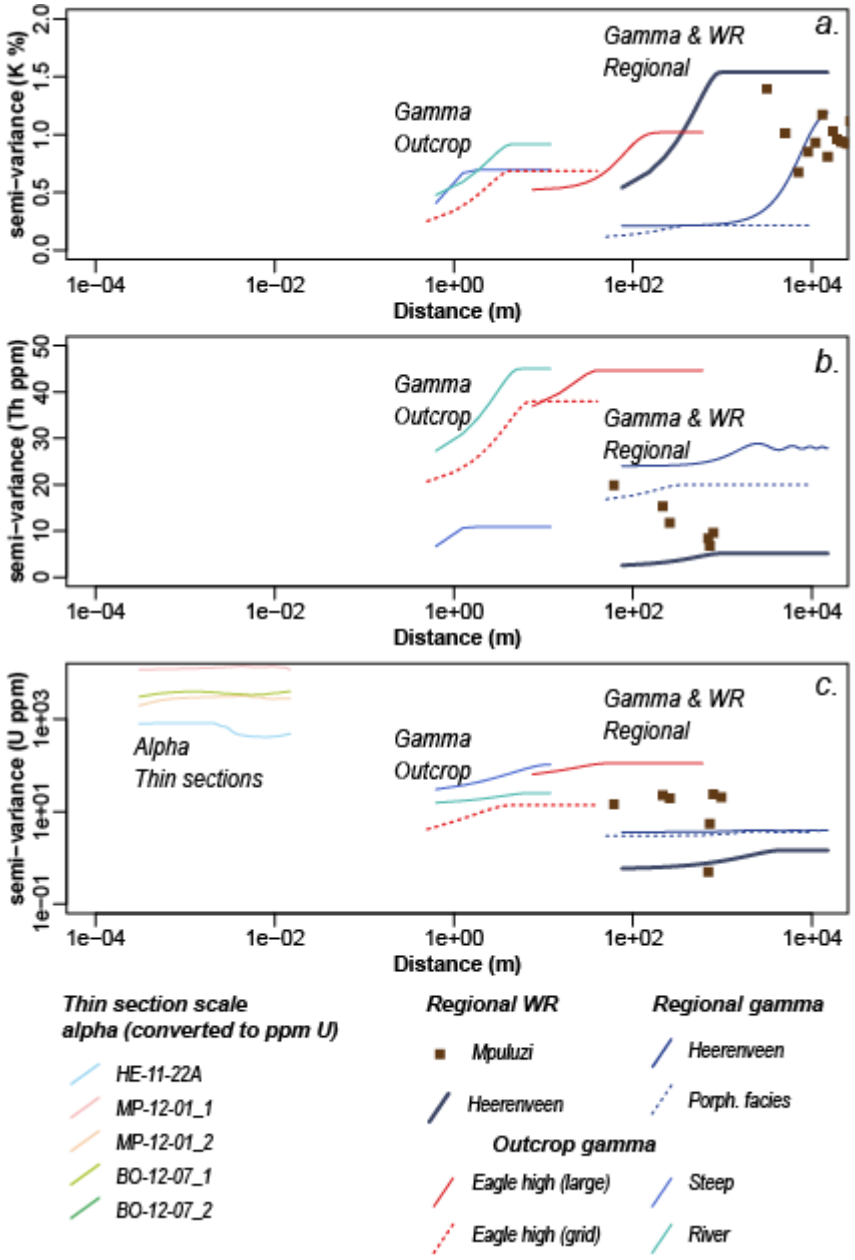

Figure 16. Compilation of the (model) variograms for the studied datasets for K (a), Th (b) and U (c). Each individual variogram (see EA6) is, for clarity, drawn using only the best fit model (lines), except for the Mpuluzi WR dataset where the variogram is too chaotic to fit a model.

Figure 16 summarizes the variograms calculated for each dataset and element, whereas individual variograms appear in Electronic Appendix EA7. Here too, the behaviours of K and U are markedly different, and reflect the different geochemical controls on both elements. Note that the empirical variograms depend on distance (by definition), but also on the sample scale. As sample scale is different between the different data sets, it is not possible to "merge" the variograms across the entire range of scales, and they are not directly comparable. In other

words, the nugget effect of a variogram obtained from a data set with large samples is not necessary equal to the sill of the variogram obtained from small scale sample. However, this figure demonstrates something that was suspected previously (Fall et al. 2018): the multiple sills and ranges of empirical variograms, across a wide range of scales, each have ramp and sill potentially reflecting different processes, operating at different scales.

Potassium generally yields smoother variograms. The nugget component of each data set is generally low. All variograms tend to have a well-defined sill. Outcrop-scale grids reach their sill after a few metres, whereas the larger ("Eagle High large" and batholith-scale) datasets only reach their sill after a few hundreds of metres. Larger-scale datasets also have larger "nugget" components that reflect the observed heterogeneities at the smaller scale. K, therefore, shows nested scales, with an outcrop-scale variability reflecting the injection of different batches of broadly similar magmas over a range of a few meters (Clemens et al., 2009). On a larger scale, more diverse magma sources (and evolution) generates a range of rock types, forming mappable (and chemically distinct) units at the batholith scale.

Here too, **uranium** shows very distinct behaviour. Variograms at all scales are dominated by strong nugget component, and the sill is only slightly above the nugget component, i.e. U concentrations are not spatially correlated but randomly distributed, and this is observed for all scales

The thin-section scale variograms yield irregular shapes that reflect the very uneven distribution of U in the thin section. Sample HE-11-22A shows an initially decreasing variogram, i.e. two close pixels are statistically more different than two pixels further away, which reflects the presence of isolated clusters of U-rich pixels in the sample, separated by large U-poor domains. Thin sections from sample MP-12-01 are still dominated by a very large nugget component, but have a poorly defined sill at scales of more than ca. 30 pixels (3 mm), reflecting the grain sizes of the uranium minerals. The thin sections from BO-12-07 (in particular section BO-12-07_2) tend to show higher variances at larger scales, despite their large nugget component. This reflects a distribution controlled by larger objects, in this case, the fracture network that is well imaged in these maps.

However, in contrast with K, the variance decreases with scale: smaller-scale datasets have a larger variance than large-scale datasets. Averaging randomly distributed compositions over larger samples will, of course, reduce the variance, as predicted by the central limit theorem

applied to U concentrations (Fall et al. 2018). This reduction of variance with the sampling scale (the size of the sample) is particularly prominent as U shows near-random distributions. Collectively, these properties reflect uranium's geochemical behaviour: it occurs only in rare (and small) grains of U-rich phases, more or less randomly distributed in the rocks at the scales investigated here (0.1 mm - 10 km).

The behaviour of **thorium** is intermediate between these two, well-defined end-members. Variograms have high nugget component, but also reach a maximum. The sills are not clearly correlated with scale. This probably reflects the behaviour of a trace element that, unlike U, substitutes in relatively common accessory phases.

8. Discussion

8.1 Gamma-ray spectrometry as a field tool

The gamma spectrometer commonly used during exploration of radioactive minerals could be much more commonly used for investigations during fundamental research field work. Despite uncertainties in our study related to calibration and analytical procedures, the device provides (semi)quantitative concentrations of the radioactive elements (K, Th and U). A significant number of analyses can be obtained over a short period of time, and directly in the field. This allows comparing, on the outcrop, differences of radioelement concentration between intrusion phases, to identify visually very similar batches of magma, to delineate hydrothermal remobilisation of radioactive elements along structures, and to select the most representative or the most "interesting" samples for further petrographic and geochemical studies.

The spectrometer also permits constructing K, U and Th distribution maps on selected outcrops by static measurements, or on a larger area by dynamic measurements using foot and/or car traverses or grids. The collected data can be interpreted during the field work, and the results can help to focus follow-up investigations without waiting for a future field season. Finally, it also permits rapid location of the most radioactive spots, which is particularly useful for mineral exploration or ore genesis studies.

On the other hand, the analyses are limited to three elements. Furthermore, even if the concentrations obtained with the spectrometer are very stable and reproducible, they differ from the whole-rock chemical analyses in area with complex rock types such as the one studied here,

with multiple units of relatively small size. This is because the measurement integrate the gamma-rays emitted from a much larger volume that the geochemical sample. In addition, the bias in the U concentration determinations may result from radioactive disequilibrium in weathered samples because we do no directly measure U but some of its decay isotopes. Therefore, spectrometric data cannot be directly compared with the whole rock geochemical data obtained from volumetrically smaller samples, unless the radioelements are relatively homogeneously distributed and U series are in secular equilibrium.

To go beyond these limitations, it would be useful to calibrate better the acquisition of gamma-ray data in imperfect field conditions. This would improve the accuracy of the results, and allow acquisition of better constrained, more quantitative data. A first step could be a simulation approach to better assess the link between the radioactive signal and the U, Th and K contents. For example, the Geant4 software is an ideal simulation tool for this kind of approach. It has recently been used to estimate the parameters for converting surface activity obtained by autoradiography (cps/mm^2) into volume activity in solids (Bq/g) (Billon et al., 2019a, b). This tool would allow assessment of the impact of geometrical and lithological parameters on gamma measurements. It would be possible to estimate the effect of (1) the distance to the ground, (2) the metallic barrier of the car, and (3) the thickness of an inactive cover (road embankment) on the measurements. Moreover, on boulders, estimation of the count as a function of the size or shape of the boulder (thickness and geometry) could be compared with count in contact with a semi-infinite medium.

In addition, the development of a new alpha and beta autoradiography field counter, currently applied to dismantling sites (MAUD project, Leblond et al, submitted) would be complementary to the use of a gamma counter. By measuring alpha particle emission, similar to what is detected by autoradiography, the results of in-situ analyses using this device would potentially better match laboratory measurements on samples.

8.2 Summary : controls on the distribution of Uranium (and other elements)

From whole thin section observations, rock geochemistry, grid measurements and detailed outcrop measurements, several types of radio-element distribution appears:

(i) The main type is related to crystal-melt fractionation, with correlative increase of U, Th and K, as expected from their incompatible behaviour in silicate melts. However, these relations are obscured in the dynamic measurements because they were performed largely in areas covered

by regolith, where U, Th and K may have experienced differential mobilisation. Uranium is easily leached from U-rich weathered rocks, K may also be leached during weathering to form clay minerals, and inversely Th is essentially bound in minerals that are resistant to weathering and may be concentrated in soils;

(ii) Another less common effect is related to aplite-pegmatite injections associated to fluid-melt fractionation and leads to a more erratic distribution of the radio-elements associated to thin pegmatite-aplite dykes, or along fracture zones. This is clearer for U, more mobile in fluids, and to a lesser extend Th. K metasomatism is also possible in some of the samples. This type of distribution is well developed in the shear zones that are developed in the eastern portion of the Heerenveen Batholith;

(iii) The third distribution is related to the remobilisation of U by oxidizing meteoric waters. Uranium can be leached from the most surficial part of the samples and redeposited as secondary hexavalent U minerals along fractures. This process is limited to rocks that contain easily leachable U minerals such as uraninite, or metamict accessory minerals. Intense alteration of the uraninite crystals with U loss was observed in the studied thin sections.

(iv) The fourth control of U distribution is well displayed at the batholith scale spectrometric measurements, with U leaching especially for the Th-richest samples, leading to very high Th/U ratios (> 10).

There is a significant spatial control on these effects. Both U and Th are concentrated in the border shear zones, but they are not always fractionated. Only particular spots within the border shear zones have low Th/U ratios. This is the combination of two effects:

- The accumulation of incompatible-element-rich phases (in the late magma batches) in these domains;
- Hydrothermal differentiation and segregation. Whereas this process occurs throughout the batholith, as shown by the patchy U distribution in the core, its effect is far more noticeable in the marginal shear zones that initially had higher background concentrations of U. Also, the shear zones act as fluid drains, such that hydrothermal effects are more pronounced there.

8.3 Multi-scale distribution of elements

The different elements investigated show strongly contrasting statistical properties. K correlates with lithological features (rock types) and shows a nearly normal distribution within a given

type, with a regular spatial distribution and scale-dependent sills. In contrast, U is related to small-scale features and far more heterogeneous and patchy, with a large nugget component. These properties reflect the very different geochemical behaviours of three incompatible elements, demonstrating that a simple classification as compatible or incompatible cannot encompass the diversity of geochemical distributions fully.

Potassium is a major element (in granitoids), i.e. it is hosted in major mineral phases of which it forms a main component (Janoušek et al., 2016). Its composition is, therefore, a direct measure of the rock types, and it correlates well with geological observations. Essentially, K can be used, at all scales, as a proxy for geological maps.

Thorium is a trace element that does not form its own mineral phases, but substitutes in other major or accessory minerals (Bea, 1996). It shows a rather complex behaviour, that reflects both the different abundances of Th in various batches of melt, and local high concentrations due to accumulation of Th-rich phases.

Th and K show clear multi-nugget sill and range patterns in their empirical variograms. This suggests that the processes dominant are not the same at all scales.

Uranium has an extreme behaviour in that it is mostly hosted in very small amounts of U-rich phases (Cuney and Friedrich, 1987), themselves primarily controlled by metre-scale processes (such as fluids circulation or fracturation). Consequently, its spatial distribution appears to be largely random at most scales of observation, with a major nugget component: the U concentration of one sample, regardless of its size, is purely a factor of chance and whether a grain of a U-bearing mineral has been included in the sample.

These findings lead to several open questions for further investigation. Firstly, can the crude typology sketched out above be extended to other elements? It is clear, for instance, that elements such as Zr behave mineralogically in a way similar to U (controlled purely by their accessory phases), but, in this case, the typical concentration of Zr is higher, and the role of fluids is smaller, so the nugget effect and strong random distributions would probably not be observed. Zr is also, indirectly, related to temperature (through the controls on zircon dissolution in melts; Watson and Harrison, 1983; Boehnke et al., 2013), so presumably the lithological control would be more pronounced. Elements such as Rb, on the other hand, while

not technically major elements, would substitute in K-bearing phases (feldspars, micas) and have a distribution similar to K. The spatial distribution of REEs would be interesting to investigate as they do not substitute (much) in major minerals but tend to form own phases (monazite, allanite, apatite).

Secondly, most of the signature that we document relates to the processes of assembly and crystallization of the batholith, with the emplacement of distinct magma batches. We do not have access to the processes responsible for the generation of these batches, and their various geochemical controls (e.g. different sources, melting, fractionation, etc.). The meaning of geochemical variations in granitoids is a hotly debated topic (e.g. Bachmann and Bergantz, 2008; Clemens et al., 2009; Gelman et al., 2014; Clemens et al., 2017; Laurent et al., 2020) and it would be interesting to see whether statistics and spatial properties could shed some light on the issue, perhaps through comparing patterns in different plutonic complexes. In theory (Allègre and Lewin, 1995), different processes (mixing, melting, fractional crystallization) should yield different distributions, and one may expect clearer spatial correlations and homogeneity in large-scale, convecting magma chambers than in collection of small magma batches.

Finally, our study covered a range of scales (Figure 5). Mapping covers scales from kilometre to 10—100 m (10-10^5 m). Laboratory work, based on thin sections, covers sub-cm scale (10^{-2} to 10^{-4} m). A gap appears at scales of 10^{-2} to 10 m, because we do not have tools that allow the description of chemical variations at cm to meter scale, a scale that is typically too small for mapping but too large for sample-based work, with rare exceptions (Belfanti, 2019). Perhaps approaches such as image analysis, portable LIBS or portable XRF (Nicoli et al., 2017) could provide some clues. A few decades ago, the use of chemically stained polished slabs was common for mapping mineral distributions (Bailey and Stevens, 1960; Couturié, 1977), and this approach may be worth revisiting, especially in combination with modern image-processing tools.

8.4 Implications for U cycling during the Archaean

The batholiths of Barberton GMS (Granite-Monzogranite-Syenite) suite are known to be more enriched in incompatible elements than the TTGs, the felsic intrusions that constitute a large part of the continental crust during the Archaean eon. One of the aims of this study was to discover whether some of those intrusions were sufficiently U-rich to permit the crystallization

of primary igneous uraninite, such as that found in the detrital placers of the later Witwatersrand Supergroup. Our study reveals that the GMS batholiths are complex objects formed by a succession of intrusive phases with different compositions, variably enriched in incompatible elements. The highest radio-element enrichments occur in the latest-emplaced magma batches, which represent a minor volumes of thes GMS complexes. Most of these granitic complexes, and especially the latest leucogranitic to pegmatitic phases that generally occur in the apical part of granitic intrusions, have probably been largely eroded away. The preservation of the U enriched granites and pegmatites of the Mpuluzi, Heerenveen and Boesmanskop tail area is probably exceptional.

The mechanisms leading to the genesis of such granitic complexes that were able to crystallize the oldest uraninite so far recorded (at 3.1 Ga) remain to be clarified. The occurrence of similar igneous rocks in other Archean cratons should also be investigated in particular by using field gamma-ray spectrometry. The discovery of such highly U-enriched granitic differentiates was quite unexpected in the Barberton Granite-Greenstone Terrain, a region which is better known as a type locality for juvenile TTG-greenstone associations. The crystallisation of uraninite at that time marks the onset of the genesis of one of the first uranium provinces on Earth, by creating the first significant uranium enrichments in the upper continental crust, at about 3.1 Ga. Then, due to its very high density and the low atmospheric oxygen levels at the time (before 2.2-2.4 Ga), uraninite was further concentrated as gravity-driven accumulations in placer deposits, as exemplified by the Dominion (3.08 Ga) and the Witwatersrand reefs (2.8-2.7 Ga) in the Witwatersrand Basin. After 2.2 Ga, during the weathering of both the uraninite-bearing granitoids and the pre-2.2 Ga placer deposits, uranium was easily solubilised and was subsequently trapped preferentially by the reducing organic rich sediments deposited in shallow-marine epicontinental environments during the Paleoproterozoic. These deposits have subsequently represented a major uranium reservoir for many types of uranium deposits (Cuney, 2010).

9. Conclusion

In this study, we investigated novel approaches to understand the geochemistry of a granitic complex. In addition to the “conventional” approach of identifying and interpreting trends on geochemical diagrams, we demonstrated the interest to take into account spatial and statistical properties.

Spatial properties (i.e. the distribution of the elements) provide additional insights into the processes that operated during the assembly of the Heerenveen batholith – in this case, the injection of late, incompatible elements-rich phases in the border shear zones, followed by fluid-mediated alteration.

Statistics help in revealing the contrasting behaviours, and hence processes that control different elements in magmatic systems. Even though K, Th and U are all incompatible, with bulk distribution coefficients in the same range (and generally speaking correlations in common binary diagrams), their distinctive statistical properties (spatial or univariate) provide additional information. Here, they reflect the differences between major elements, trace elements controlled by substitution in relatively common (main or accessory) phases and trace elements controlled by rare accessory phases.

We also established the importance of using in-situ analytical techniques, such as gamma-ray spectrometry, for the study of granitoids. Although the range of elements available is restricted, and the data are semi-quantitative, some features render this approach particularly useful. Firstly, the speed of acquisition – an analysis takes a few minutes at most, producing far faster results than sampling, packing, analysing, etc. The very low cost (effectively zero, if the equipment is available) of these analyses is also an important aspect. Secondly, it alleviates the need to physically sample; depending on the context, this may be an asset, as in the case of the Heerenveen Batholith where typical outcrops are flat surfaces, the sampling of which is difficult. It could also be beneficial in logistically challenging situations, in which transportation of large volumes of rocks would be an issue, in historically sensitive sites that cannot be hammered, and so on. Thirdly and more fundamentally, a systematic survey represents random sampling, unbiassed by sampling strategy or sample availability. If nothing else, such an approach is complementary to more conventional strategies, and at least allows checking that the conclusions are globally tenable.

We do not claim that tools such as statistics or gamma-ray mapping should replace the time-honoured approach based on interpretation of trends and laboratory analyses. However, we do propose that they offer a complementary view that allows, at a relatively limited cost, improved understanding of igneous systems. As such, the "crustal petrology" community would benefit from a more widespread application of these tools.

Supplementary electronic material

Electronic appendices for this paper are available for review at:
https://www.dropbox.com/sh/psdrbjmp9l8t17d/AABcWM8YVVtn7vBpsXVNZP5Da?dl=0

EA1 (Excel). Whole-rock analyses for Heerenveen and Mpuluzi batholiths
EA2 (Excel). Details on reproducibility analysis.
EA3 (Excel). Raw gamma-ray data, for the different datasets used.
EA4 (zip, includes images). BeaQuant maps, unprocessed.
EA5 (zip, various files). Input files and R scripts used for processing.
EA6 (pdf). Univariate statistics for individual datasets.
EA7 (pdf). Variograms for individual datasets.

Acknowledgments

We thank ORANO (formerly AREVA), and in particular Jean-Marc Miehe, for lending us a gamma-ray spectrometer during the 2012 field campaign. Alex Kisters (Stellenbosch) and his students (G. Sonke and C. Campbell, and in particular R. Belcher) kindly supplied detailed maps of the Eagle High outcrop – in addition to introducing me (JFM), long ago, to the geology of the GMS granitoids and sharing their best outcrops. Land owners in the Heerenveen and Mpuluzi batholiths, and in particular at Eagle High, were very welcoming and helpful and generously allowed access to their land. Céline Boissard (IC2MP, Poitiers) is warmly thanked for her help for SEM thin-section imaging. Suggestions by M. Jébrak on a previous version of this work, and extensive and detailed reviews by two anonymous reviewers, greatly improved the final manuscript.

This work was financially supported by several CNRS/INSU grants (PNP and CESSUR). JFM's stay at Monash was supported by the Australian Research Council grant FL160100168. This is IRP BuCoMo contribution A10 (2020).

It is a great honour to contribute to this Special Issue celebrating Carl Anhaeusser's achievements. After nearly 20 years working in Barberton, I (JFM) still regularly run into parts of Carl's work that I was not aware of, and, more often than not, I find that some of my best ideas (or so I think) have already been published in an Anhaeusser et al. paper. My sad excuses for maps are no match for Carl's amazing mapping work, especially in complex

granite/migmatite/greenstone terrain. The databases he assembled (with L. Robb) on Barberton granitoids remain, to this day, some of the most comprehensive in existence on Barberton rocks, and remain the foundation of most of my data-mining efforts. It is, therefore, a privilege to offer this contribution, which combines geochemical datasets with spatial analysis in an effort to go, perhaps, beyond mapping.

References

Agterberg, F.P., 2012. Multifractals and geostatistics. Journal of Geochemical Exploration 122, 113–122. https://doi.org/10.1016/j.gexplo.2012.04.001.

Aitchison, J., 1986. The statistical analysis of compositional data. Methuen, New York.

Allegre, C.J., Lewin, E., 1995. Scaling laws and geochemical distributions. Earth and Planetary Science Letters 132, 1-13.

Angileri, A., Sardini, P., Beaufort, D., Amiard, G., Beaufort, M.F., Nicolai, J., Siitari-Kauppi, M., Descostes, M., 2020, Mobility of daughter elements of 238U decay chain during leaching by In Situ Recovery (ISR): New insights from digital autoradiography, Journal of Environmental Radioactivity 220-221.

Angileri, A., Sardini, P., Donnard, J., Duval, S., Lefeuvre, H., Oger, T., Patrier, P., Rividi, N., Siitari-Kauppi, M., Toubon, H., 2018. Mapping 238U decay chain equilibrium state in thin sections of geo-materials by digital autoradiography and microprobe analysis. Applied Radiation and Isotopes 140, 228-237.

Anhaeusser, C.R., Robb, L.J., 1983. Geological and geochemical characteristics of the Heeenveen and Mpuluzi batholiths south of the Barberton greenstone belt, and preliminary thoughts on their petrogenesis, Contributions to the geology of the Barberton Mountain land. Geological Society of South Africa, pp. 131-151.

Bachmann, O., Bergantz, G.W., 2008. Rhyolites and their source mushes across tectonic settings. Journal of Petrology 49, 2277-2285.

Bailey, E.H., Stevens, R.E., 1960. Selective staining of K-feldspar and plagioclase on rock slabs and thin sections. American Mineralogist: Journal of Earth and Planetary Materials 45, 1020-1025.

Baratoux, D., Jessell, M.J., McFarlane, H., Fall, M., André-Mayer, A.S., Vanderhaegue, O., Baratoux, L., Boamah, K., Ndiaye, P.M., 2015. Crustal distribution of K/Th on Earth and Mars, Goldschmidt Conference, Prague.

Baratoux, D., Jessell, M.W., Fall, M., Ndiaye, P.M., Vanderhaeghe, O., Baratoux, L., McFarlane, H., Boamah, K., Andre-Mayer, A.S., in revision. Crustal differentiation on Earth and Mars from Potassium and Thorium multi-scale distributions. Nature Communications.

Bea, F., 1996. Residence of REE, Y, Th and U in Granites and Crustal Protoliths; Implications for the Chemistry of Crustal Melts. Journal of Petrology 37, 521-552.

Belcher, R.W., Kisters, A.F.M., 2006a. Progressive adjustments of ascent and emplacement controls during incremental construction of the 3.1 Ga Heerenveen batholith, South Africa. Journal of Structural Geology 28, 1406-1421.

Belcher, R.W., Kisters, A.F.M., 2006b. Syntectonic emplacement and deformation of the Heerenveen batholith: conjectures on the structural setting of the 3.1 Ga granite magmatism in the Barberton granite-greenstone terrain, South Africa. Geological society of America special Publication 405, 211-231.

Belfanti, S.A., 2019. Feldspar Megacrysts as a Window into the Crystallization of Silicic Magmas: A Study in The Tuolumne Intrusive Complex, Yosemite National Park, CA. Vanderbilt University.

Belousova, E., Griffin, W.L., O'Reilly, S.Y., Fisher, N., 2002. Igneous zircon: trace element composition as an indicator of source rock type. Contributions to Mineralogy and Petrology 143, 602-622.

Bierwirth, P.N., Brodie, R.S., 2008. Gamma-ray remote sensing of aeolian salt sources in the Murray–Darling Basin, Australia. Remote Sensing of Environment 112, 550–559. https://doi.org/10.1016/j.rse.2007.05.012

Billon, S., Sardini, P., Angileri, A., Beaucaire, C., Parneix, J.C., Siitari-Kauppi, M., Descostes, M., 2020. Quantitative imaging of 226Ra ultratrace distribution using digital autoradiography: Case of doped celestines. Journal of Environmental Radioactivity 217, 106211.

Billon, S., Sardini, P., Leblond, S., Fichet, P., 2019a. From Bq cm− 3 to Bq cm− 2 (and conversely)—part 1: a useful conversion for autoradiography. Journal of Radioanalytical and Nuclear Chemistry 320, 643-654.

Billon, S., Sardini, P., Leblond, S., Fichet, P., 2019b. From Bq cm− 3 to Bq cm− 2 (and conversely)—part 2: useful dataset to apply the conversion to decommissioning operations. Journal of Radioanalytical and Nuclear Chemistry 320.

Boehnke, P., Watson, E.B., Trail, D., Harrison, T.M., Schmitt, A.K., 2013. Zircon saturation re-revisited. Chemical Geology 351, 324-334.

Bonin, B., Janousek, V., Moyen, J.F., 2019. Chemical variation, modal composition and classification of granitoids, in: Janousek, V., Bowden, P., Bonin, B., Fiannacca, P. (Eds.), Post-

Archean Granitic Rocks: Petrogenetic Processes and Tectonic Environments. Geological Society of London.

Bouchez, J.L., Delas, C., Gleizes, G., Nedelec, A. & Cuney, M. 1992. Submagmatic Microfractures in Granites. Geology, 20, 35-38.

Clemens, J., Stevens, G., Frei, D., Joseph, C., 2017. Origins of cryptic variation in the Ediacaran–Fortunian rhyolitic ignimbrites of the Saldanha Bay Volcanic Complex, Western Cape, South Africa. Contributions to Mineralogy and Petrology 172, 99.

Clemens, J.D., Belcher, R.W., Kisters, A.F.M., 2010. The Heerenveen Batholith, Barberton Mountain Land, South Africa: Mesoarchaean, Potassic, Felsic Magmas Formed by Melting of an Ancient Subduction Complex. Journal of Petrology 51, 1099.

Clemens, J.D., Helps, P.A., Stevens, G., 2009. Chemical structure in granitic magmas - a signal from the source? Transactions of the Royal Society of Edinburgh-Earth Sciences 100, 159-172.

Couturie, J.P., 1977. Le massif granitique de la Margeride (Massif Central Français). UER de sciences exactes et naturelles, Université Clermont II, Clermont-Ferrand.

Cressie, N., 1992. Statistics for spatial data. Terra Nova 4, 613-617.

Cuney, M. 2014. Felsic magmatism and uranium deposits. Bulletin de la Société Géologique de France, 185, 75-92.

Cuney, M., 2010. Evolution of uranium fractionation processes through time: driving the secular variation of uranium deposit types. Economic Geology 105, 553-569.

Cuney, M., 2020. Nuclear Geology, in: Elias, S.A., Alderton, D. (Eds.), Encyclopedia of Geology, 2nd ed.

Cuney, M., Friedrich, M., 1987. Physicochemical and Crystal-Chemical Controls on Accessory Mineral Paragenesis in Granitoids - Implications for Uranium Metallogenesis. Bulletin de Mineralogie 110, 235-247.

Cuney, M., Friedrich, M., Blumenfeld, P., Bourguignon, A., Boiron, M., Vigneresse, J., Poty, B., 1990. Metallogenesis in the French part of the Variscan orogen. Part I: U preconcentrations in pre-Variscan and Variscan formations--a comparison with Sn, W and Au. Tectonophysics 177, 39-57.

Cuney, M., Kyser, K., 2015. Radioactivity, Heat Production and Natural Reactors, in: Cuney, M., Kyser, K. (Eds.), Geology and geochemistry of uranium and thorium deposits. Mineralogical Association of Canada.

Cuney, M., Kyser, T., 2009. Recent and not-so-recent developments in uranium deposits and implications for exploration. Mineralogical Association of Canada.

Dentith, M., Mudge, S.T., 2014. Geophysics for the mineral exploration geoscientist. Cambridge University Press.

Depiné, M., Frimmel, H., Emsbo, P., Koenig, A., Kern, M., 2013. Trace element distribution in uraninite from Mesoarchaean Witwatersrand conglomerates (South Africa) supports placer model and magmatogenic source. Mineralium Deposita 48, 423-435.

De Wijs, H.J., 1951. Statistics of ore distribution, part I. Geologie en Mijnbouw 13, 365–375.

Dickson, B.L., Scott, K.M., 1997. Intepretation of aerial gamma-ray surveys-adding the geochemical factor. AGSO Journal of Australian Geology & Geophysics 17, 187–200.

Donnard, J., Arlicot, N., Berny, R., Carduner, H., Leray, P., Morteau, E., Servagent, N., Thers, D., 2009a. Advancements of labelled radio-pharmaceutics imaging with the PIM-MPGD. Journal of Instrumentation 4, 11022-11022.

Donnard, J., Berny, R., Carduner, H., Leray, P., Morteau, E., Provence, M., Servagent, N., Thers, D., 2009b. The Micro-Pattern Gas Detector PIM: a multi-modality solution for novel investigations in functional imaging. Nuclear Instruments and Methods in Physics Research Section A: Accelerators, Spectrometers, Detectors and Associated Equipment 610, 158-160.

Duhamel, I., 2010. Caractérisation des sources d'uranium à l'Archéen: mécanismes de genèse des gisements d'uranium les plus anciens (3, 0 à 2, 2 Ga) et des préconcentrations uranifères paléoprotérozoïques. Nancy 1.

Elkhateeb, S.O., Abdellatif, M.A.G., 2018. Delineation potential gold mineralization zones in a part of Central Eastern Desert, Egypt using Airborne Magnetic and Radiometric data. NRIAG Journal of Astronomy and Geophysics 7, 361–376. https://doi.org/10.1016/j.nrjag.2018.05.010

Fall, M., Baratoux, D., Jessell, M., Moussa Ndiaye, P., Vanderhaeghe, O., Moyen, J.-F., Baratoux, L., Bonzi, W.M.E., in press. The redistribution of thorium, uranium, potassium by magmatic and hydrothermal processes versus surface processes in the Saraya Batholith (Eastern Senegal): insights from airborne radiometrics data and topographic roughness. Journal of Geochemical Exploration.

Fall, M., Baratoux, D., Ndiaye, P.M., Jessell, M., 2018. Multi-scale distribution of Potassium, Thorium and Uranium in Paleoproterozoic granites from eastern Senegal. Journal of African Earth Sciences and the Middle East in press.

Foerster, H.-J., 1998. The chemical composition of REE-Y-Th-U-rich accessory minerals in peraluminous granites of the Erzgebirge-Fichtelgebirge region, Germany; Part I, The monazite-(Ce)-brabantite solid solution series. American Mineralogist 83, 259-272.

Förster, H.-J., 2006. Composition and origin of intermediate solid solutions in the system thorite–xenotime–zircon–coffinite. Lithos 88, 35-55.

Debon, F. & Lefort, P. 1983. A chemical–mineralogical classification of common plutonic rocks and associations. Transactions of the Royal Society of Edinburgh: Earth Sciences, 73.

Gelman, S.E., Deering, C.D., Bachmann, O., Huber, C., Gutierrez, F.J., 2014. Identifying the crystal graveyards remaining after large silicic eruptions. Earth and Planetary Science Letters 403, 299-306.

Greenberger, R.N., Ehlmann, B.L., Osinski, G.R., Tornabene, L.L., Green, R.O., 2020. Compositional Heterogeneity of Impact Melt Rocks at the Haughton Impact Structure, Canada: Implications for Planetary Processes and Remote Sensing. J. Geophys. Res. Planets. https://doi.org/10.1029/2019JE006218.IAEA, 2003. Guidelines for radioelement mapping using gamma ray spectrometry data. IAEA, Vienna.

Janoušek, V., Moyen, J.F., Martin, H., Erban, V., Farrow, C.M., 2016. Geochemical Modelling of Igneous Processes—Principles and Recipes in the R Language. Springer Verlag, Berlin.

Kelsey, D.E., Clark, C. & Hand, M. 2008. Thermobarometric modelling of zircon and monazite growth in melt–bearing systems: examples using model metapelitic and metapsammitic granulites. Journal of Metamorphic Geology, 26, 199-212.

Krupp, R., Oberthuer, T., Hirdes, W., 1994. The early Precambrian atmosphere and hydrosphere; thermodynamic constraints from mineral deposits. Economic Geology 89, 1581-1598.

Laurent, O., Björnsen, J., Wotzlaw, J.-F., Bretscher, S., Pimenta Silva, M., Moyen, J.F., Ulmer, P., Bachmann, O., 2020. Earth's earliest granitoids are crystal-rich magma reservoirs tapped by silicic eruptions. Nature Geoscience.

Leblond, S., Fichet, P., Laumonier, R., Billon, S., Sardini, P., accepted with revision. Development of a compact alpha and beta camera for dismantlement applications, Nuclear Instruments and Methods in Physics Research Section A: Accelerators, Spectrometers, Detectors and Associated Equipment.

Lumpkin, G.R., Ewing, R.C., 1996. Geochemical alteration of pyrochlore group minerals: Betafite subgroup. American Mineralogist 81, 1237-1248.

Marsh, J.S., 2006. The Dominion group, The Geology of South Africa. Council for Geoscience, Pretoria, pp. 149-154.

Mavi, B., 2012. Experimental investigation of γ-ray attenuation coefficients for granites. Annals of Nuclear Energy 44, 22-25.

Metelka, V., Baratoux, L., Jessell, M.W., Barth, A., Ježek, J., Naba, S., 2018. Automated regolith landform mapping using airborne geophysics and remote sensing data, Burkina Faso,

West Africa. Remote Sensing of Environment 204, 964–978. https://doi.org/10.1016/j.rse.2017.08.004

Minter, W.E.L., 2006. The sedimentary setting of Witwatersrand placer mineral deposits in an Archean atmosphere. Memoirs-Geological Society of America 198, 105.

Montel, J.-M. 1993. A model for monazite/melt equilibrium and application to the generation of granitic magmas. Chemical Geology, 110, 127-146.

Moyen, J.-F., Stevens, G., Kisters, A.F.M., Belcher, R.W., Lemirre, B., 2018. TTG plutons of the Barberton granitoid-greenstone terrain, South Africa, in: Van Kranendonk, M., Bennett, V., Hoffmann, J.E. (Eds.), Earth Oldest Rocks, 2nd ed. Elsevier, pp. 615-654.

Moyen, J.-F., Zeh, A., Cuney, M., Dziggel, A., Carrouée, S., in press. The multiple ways of recycling Archaean crust : a case study from the ca. 3.1 Ga granitoids from the Barberton Greenstone Belt, South Africa. Precambrian Research.

Negga, H., Sheppard, S., Rosenbaum, J., Cuney, M., 1986. Late Hercynian U-vein mineralization in the Alps: fluid inclusion and C, O, H isotopic evidence for mixing between two externally derived fluids. Contributions to Mineralogy and Petrology 93, 179-186.

Nicoli, G., Stevens, G., Moyen, J.F., Vézinet, A., Mayne, M., 2017. Insights into the complexity of crustal differentiation from K2O-poor leucosomes within metapelitic migmatites: Southern Marginal Zone of the Limpopo Belt, South Africa. Journal of Metamorphic Geology 35, 999-1022.

Partin, C., Lalonde, S.V., Planavsky, N., Bekker, A., Rouxel, O., Lyons, T., Konhauser, K., 2013. Uranium in iron formations and the rise of atmospheric oxygen. Chemical Geology 362, 82-90.

Pawlowsky-Glahn, V., Egozcue, J.J., 2006. Compositional data and their analysis: an introduction. Geological Society, London, Special Publications 264, 1-10.

Pebesma, E.J., 2004. Multivariable geostatistics in S: the gstat package. Computers & Geosciences 30, 683-691.

Phillips, G., Law, J., 1997. Hydrothermal origin for Witwatersrand gold. Society of Economic Geology, Newsletter 31.

Rantzsch, U., Gauert, C.D., Van der Westhuizen, W.A., Duhamel, I., Cuney, M., Beukes, G.J., 2011. Mineral chemical study of U-bearing minerals from the Dominion Reefs, South Africa. Mineralium Deposita 46, 187-196.

Robb, L., Charlesworth, E., Drennan, G., Gibson, R., Tongu, E., 1997. Tectono-metamorphic setting and paragenetic sequence of Au-U mineralisation in the Archaean Witwatersrand Basin, South Africa. Australian Journal of Earth Sciences 44, 353-371.

Robb, L.J., Meyer, F.M., 1995. The Witwatersrand Basin, South Africa: geological framework and mineralization processes. Ore Geology Reviews 10, 67-94.

Sardini, P., Angileri, A., Descostes, M., Duval, S., Oger, T., Patrier, P., Rividi, N., Siitari-Kauppi, M., Toubon, H., Donnard, J., 2016. Quantitative autoradiography of alpha particle emission in geo-materials using the Beaver™ system. Nuclear Instruments and Methods in Physics Research Section A: Accelerators, Spectrometers, Detectors and Associated Equipment 833, 15-22.

Silverman, B.W., 1986. Density estimation. Chapman and Hall, London.

Škoda, R., Novák, M., 2007. Y, REE, Nb, Ta, Ti-oxide (AB2O6) minerals from REL–REE euxenite-subtype pegmatites of the Třebíč Pluton, Czech Republic; substitutions and fractionation trends. Lithos 95, 43-57.

Smits, G., 1989. (U-Th)-bearing silicates in reefs of the Witwatersrand, South Africa. The Canadian Mineralogist 27, 643-656.

Sonke, G.-J., 2006. Internal architecture of the sheeted margin of the 3.1 Ga Mpuluzi batholith, Barberton granite-greenstone terrain., Dept of Geology. Stellenbosch University, Stellenbosch.

Tartèse, R., Boulvais, P., Poujol, M., Vigneresse, J.-L., 2011. Granite petrogenesis revealed by combined gravimetric and radiometric imaging. Tectonophysics 501, 98-103.

Venables, W.N., Ripley, B.D., 2002. Modern Applied Statistics with S. Springer.

Watson, E.B., Harrison, T.M., 1983. Zircon saturation revisited: temperature and composition effects in a variety of crustal magmas types. Earth and Planetary Science Letters 64, 295-304.

Xhixha, M.K., Albèri, M., Baldoncini, M., Bezzon, G.P., Buso, G.P., Callegari, I., Casini, L., Cuccuru, S., Fiorentini, G., Guastaldi, E., Mantovani, F., Mou, L., Oggiano, G., Puccini, A., Alvarez, C.R., Strati, V., Xhixha, G., Zanon, A., 2016. Uranium distribution in the Variscan Basement of Northeastern Sardinia. Journal of Maps 12, 1029–1036. https://doi.org/10.1080/17445647.2015.1115784

Yearron, L.M., 2003. Archaean granite petrogenesis and implications for the evolution of the Barberton Mountain Land, South Africa. Kingston University, Kingston, UK, p. 315.

Yokoyama, E., Nédélec, A., Baratoux, D., Trindade, R.I.F., Fabre, S., Berger, G., 2015. Hydrothermal alteration in basalts from Vargeão impact structure, south Brazil, and implications for recognition of impact-induced hydrothermalism on Mars. Icarus 252, 347–365. https://doi.org/10.1016/j.icarus.2015.02.001